Available online at www.sciencedirect.com
ScienceDirect
European Journal of Mechanics B/Fluids 26 (2007) 551–582

Testing of Reynolds-stress-transport closures by comparison with DNS of an idealized adverse-pressure-gradient boundary layer

M.A. Sciberras, G.N. Coleman *

School of Engineering Sciences, University of Southampton, SO17 1BJ, UK

Received 5 May 2006; received in revised form 30 September 2006; accepted 8 November 2006

Available online 13 December 2006

Abstract

Results are used from direct numerical simulation (DNS) of incompressible plane-channel flow subjected to a uniform straining field typical of a two-dimensional adverse pressure gradient (APG) to investigate the accuracy of three second-moment closures specially designed to account for wall-bounded turbulence. Since the DNS statistics satisfy a one-dimensional unsteady problem with rigorously defined boundary and initial conditions, and since the flow contains many of the essential features found in suddenly decelerated boundary layers, this allows an efficient and straightforward but non-trivial assessment of the closures. The Reynolds-stress budgets from the DNS are used to examine the individual production/dissipation/transport terms used by each closure. This reveals shortcomings in all three schemes, especially in the near-wall behavior of their pressure–strain models. One of the major findings of this study is the degree to which the individual modeling shortcomings are offset by the tendency for them to cancel each other. The Wilcox Stress-ω model best captures the cumulative effect of the APG straining, compared to the models of Launder and Shima and So et al., in terms of giving mean velocities and the time at which the surface shear stress reverses sign that most closely agree with the DNS. However, its prediction of the streamwise $\overline{u'u'}$ and wall-normal $\overline{v'v'}$ Reynolds stresses is much less accurate than that given by the other two schemes.

Keywords: Turbulence models; Second-moment closures; Wall-bounded turbulence; Adverse-pressure-gradient boundary layers; Strained-channel DNS)

1. Introduction

This article examines the ability of second-order Reynolds-averaged Navier–Stokes (RANS) closures to predict the response of wall-bounded turbulence to two-dimensional (2D) strains associated with a suddenly applied adverse pressure gradient (APG). We compare three 'off-the-shelf' models with data from a direct numerical simulation (DNS) of a 'strained-channel' flow, a time-dependent parallel-flow idealization of the spatially developing decelerated boundary layer. This study is similar to that of Yorke and Coleman [1], who focused on the performance of popular lower-order models for this 2D APG case.

The strained-channel approach has the advantage of emulating perturbed turbulent boundary layers with a flow whose statistics depend only on time and one spatial dimension. Given the information available from DNS (such as

* Corresponding author.
E-mail address: g.n.coleman@soton.ac.uk (G.N. Coleman).

0997-7546/$ – see front matter
doi:10.1016/j.euromechflu.2006.11.001

Reynolds-stress budgets), this provides a rigorous but quick and efficient test for the models. Because it captures many of the essential characteristics of perturbed spatial layers (see Section 2), the strained-channel analogue provides a non-trivial modeling challenge. Yorke and Coleman [1] found that the Baldwin–Lomax (algebraic), Spalart–Allmaras (one-equation), Launder–Sharma and Menter SST (both two-equation) models each give significantly different predictions of the history of the wall-shear stress and evolution of the Reynolds-stress profiles, when applied to the APG-strained channel (Spalart–Allmaras and Menter SST give the best overall agreement with the DNS, although they leave room for improvement in their predictions of some statistics). This motivates the current examination of the Reynolds-stress transport models, which were chosen because they are relatively new and also represent distinct modeling strategies for wall-bounded flows. We will examine how well the closures reproduce the APG-induced skin-friction reversal and the finite-time lag required for the turbulence to respond to sudden mean-flow changes. Besides checking the overall model performance for low-order statistics, we also use Reynolds-stress budgets from the DNS to examine the individual production/dissipation/transport terms of the three models tested.

An overview of the strained-channel methodology and the resulting DNS benchmark is presented in Section 2, while Section 3 summarizes the three subject closures and the code used for their solution (details are included in Appendix A). Model-DNS comparisons are given in the following section, for both unstrained plane-channel flow (Section 4.1) and the idealized 2D APG (Section 4.2); a recap of the results and their implications is given in Section 4.3. We conclude in Section 5 with a summary and closing comments.

2. 2D APG strained-channel DNS

The second-order closures are to be tested by comparing them with DNS of an idealized APG boundary layer – namely turbulent plane channel flow subjected to a uniform irrotational mean strain and simultaneous time-dependent in-plane wall motion (Fig. 1). In this idealization, convective changes in the spatial boundary layer are replaced by temporal ones in the parallel-flow plane channel. An overview of this approach follows, as applied to the APG strain considered here; a fuller explanation for more general 2D and 3D strains is given in [2,3]. We also include a summary of the DNS results to which the models will be compared (some of the figures and text in this section were also used in [1]).

The objective of the strained-channel approach is to subject turbulence in the core of a plane channel to the same straining history it would experience if it were in the outer layer of an actual, spatially developing, APG boundary layer. Fully developed statistically stationary incompressible wall-bounded turbulence is subjected to a steady uniform irrotational divergence-free strain field $A_{ij} = \partial U_i/\partial x_j$ with streamwise deceleration A_{11} and wall-normal divergence A_{22}, such that

$$A_{ij} = \begin{bmatrix} A_{11} & 0 & 0 \\ 0 & A_{22} & 0 \\ 0 & 0 & 0 \end{bmatrix} = \begin{bmatrix} \partial U/\partial x & 0 & 0 \\ 0 & \partial V/\partial y & 0 \\ 0 & 0 & 0 \end{bmatrix}, \tag{2.1}$$

where $A_{11} = -A_{22} < 0$. A simple step-function time history is applied, in which A_{ij} is zero until time $t = 0$ and then constant thereafter. The strained-channel domain is periodic in the streamwise x and spanwise z directions, and

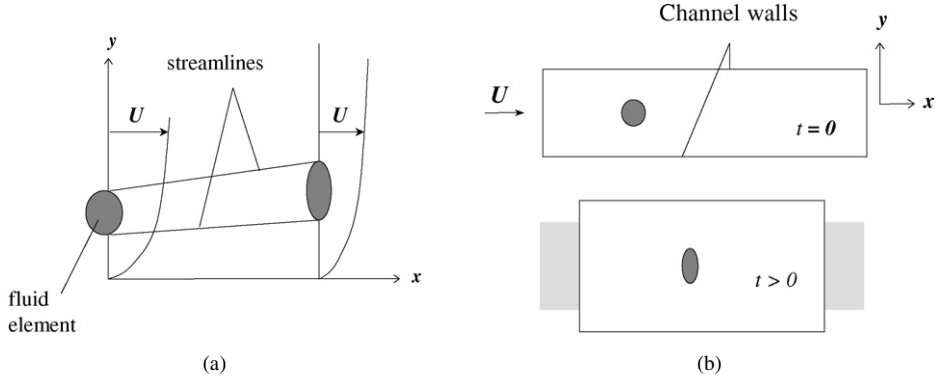

Fig. 1. Side view of 2D APG boundary layer. (a) Spatially developing flow. (b) Initial and deformed domain of time-developing strained-channel idealization (from [3]).

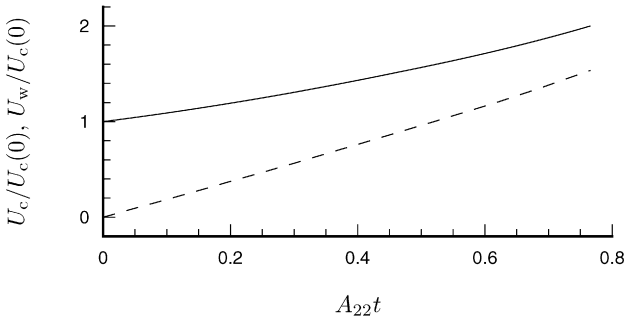

Fig. 2. Histories of mean centerline U_c and wall U_w velocities from APG-strained channel DNS [3]: —, U_c; - - -, U_w.

has two no-slip flat (but elastic) parallel walls; the y coordinate denotes the wall-normal direction. The fact that A_{ij} is uniform in y will maintain a rectangular domain, as required by the DNS code (it also leads to the flat no-slip walls being strained along with the fluid between them; see [2,3]). At the same time that the irrotational strain is applied, the deforming channel walls are also set in motion in their own plane, in order to duplicate the deceleration induced by the spatial APG on the bulk flow. The ensuing temporal variation of the mean spanwise vorticity at the channel walls approximates the corresponding near-wall variation experienced in the spatial boundary layer. The history of the in-plane wall velocity $U_w(t)$ is set by A_{11} and the mean time-dependent centerline channel velocity $U_c(t)$ (which also depends on A_{11}), by equating the convective and temporal changes in the outer layer: we assume $\mathrm{d}(U_c - U_w)/\mathrm{d}t = U_c A_{11}$ (see Eq. (2.3) and Fig. 2). In this way we are able to account for both the inner-layer (rotational) and outer-layer (irrotational) deformations induced in a spatial boundary layer by an APG.

DNS of this flow has been performed for the case where the APG strain (2.1) is imposed upon a precursor plane-channel DNS at friction-velocity Reynolds number $Re_\tau = u_\tau h/\nu = 390$, with $A_{11} = -A_{22} = 0.31 u_\tau(0)/h(0)$, where $u_\tau(0)/h(0)$ is the ratio of the initial values of the friction velocity $u_\tau(t)$ to the channel half-width $h(t)$. A full discussion of the DNS data and numerical procedures – including generation of the time-dependent statistics (ensemble averaged and 'folded' about the centerline), and the spatial discretization and computation resources – is presented in [3]. Representative results are shown in Fig. 3. These first- and second-order statistics, which will be used to evaluate the accuracy of the selected closures, are from a 21-field ensemble average,[1] at $A_{22}t = 0$, 0.19 and 0.365. The symbols in Fig. 3(a), (b) are from a single realization (i.e. x–z plane average and doubling) at $A_{22}t = 0.77$ – a time after which a small near-wall reverse-flow region forms. (Second-order statistics for $A_{22}t = 0.77$ are not shown, since they contain large unphysical statistical oscillations due to the incomplete single-field sample. Finite CPU resources did not allow the full 21-field average to be advanced from $A_{22}t = 0.365$ to 0.77.)

Features of APG boundary layers [4,5] observed in the DNS include the increase of layer thickness and reduction of bulk mass flow and wall shear stress, seen in the mean velocity evolution (Fig. 3(a)). The shape factor (in terms of the displacement and momentum thicknesses in the half-channel) increases from $H = \delta^*/\theta = 1.45$ at $A_{22}t = 0$ to $H = 1.70$ at $A_{22}t = 0.365$ and $H = 2.50$ at $A_{22}t = 0.77$ (just after the skin friction has changed sign; cf. Fig. 13). The latter value is close to the $H \approx 2.7$ found at separation by Alving and Fernholz [6] in their axisymmetric-body separation-bubble experiment. The effective Clauser pressure-gradient parameter increases from $\beta_{\mathrm{eff}} = -\delta^*(U_c - U_w)A_{11}/u_\tau^2 = 0.78$ at $A_{22}t = 0$, to 5.7 at $A_{22}t = 0.365$, and then infinity. The flow is thus far from a constant-β 'equilibrium' regime, for which one could expect similarity of the outer-layer mean-velocity defect [7]. It is also well away from the rapid-distortion regime. Fig. 3(b) shows the relative importance of the applied strain, compared to the mean shear $\partial\bar{u}/\partial y$ at each wall-normal location y_w. We note that A_{22} is at least an order of magnitude smaller than $|\partial\bar{u}/\partial y|$ over the entire channel (except near the centerline, where $\partial\bar{u}/\partial y \to 0$) for all times considered, including just after the wall-shear stress has changed sign. On the other hand, Fig. 3(c) shows that the timescale defined by the mean

[1] Although 21 fields are not enough to remove all statistical uncertainty from the results (especially for quantities involving differences between much larger terms, such as the net rate of change of the Reynolds-stress budgets $\partial\overline{u_i'u_j'}/\partial t$ – see e.g. the open symbols in Figs. 4(a) and 5(a)), they are sufficient to reveal quantitative trends against which the closures can be meaningfully compared. This was verified by comparing the $\partial\overline{u_i'u_j'}/\partial t$ given by the sum of the budget terms with the actual temporal variation observed in the Reynolds-stress profiles.

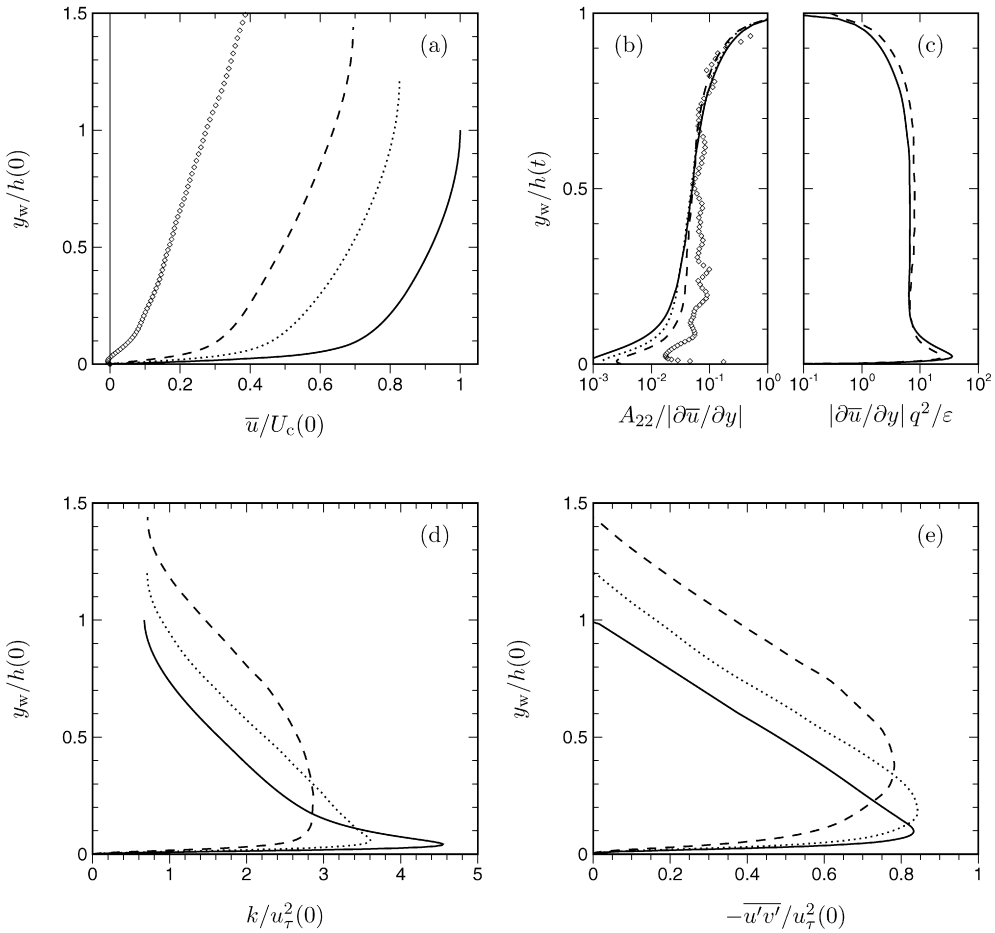

Fig. 3. DNS profiles of (a) mean velocity, (b), (c) timescale ratios, (d) kinetic energy and (e) Reynolds shear stress: —, $A_{22}t = 0$; ···, $A_{22}t = 0.19$. - - -, $A_{22}t = 0.365$. ⋄, $A_{22}t = 0.77$ (single realization). Mean velocities in (a) measured with respect to coordinate system attached to streamwise moving walls (cf. Fig. 2). Distance to the nearest wall $y_w = |y - h|$. Results from [3].

shear is everywhere of the same order as the 'eddy turn-over' time q^2/ε (where $k = \frac{1}{2}\overline{u_i' u_i'} = \frac{1}{2}q^2$ is the turbulence kinetic energy and ε its rate of dissipation). The magnitude of the applied strain is thus not large enough, at any y_w, to overwhelm the non-linear 'self-interaction' processes of the turbulence. This hints at the challenge this flow provides for one-point closures, since it will for example exercise both the 'rapid' and 'slow' terms in Reynolds-stress transport models.

Other APG characteristics that are duplicated are the near-wall reduction, and outer-layer increase [4], of turbulence intensity, illustrated by the turbulence kinetic energy k and Reynolds shear stress $-\overline{u'v'}$ (Figs. 3(d), (e)). The effect of the applied strain upon the individual terms in the $-\overline{u'v'}$ and $\overline{v'v'}$ Reynolds-stress budgets is shown (via the shaded regions) in Figs. 4 and 5 (the terms are defined in Section 3). Also shown for both the unstrained and strained cases are the pressure–strain ($-\phi_{12}$ and ϕ_{22}) and pressure–diffusion (ψ_{12} and ψ_{22}) terms into which the velocity–pressure-gradient correlations $-\Pi_{12}$ and Π_{22} are commonly decomposed (see Eq. (3.4)). (The modeling implications of using this decomposition will be considered below. For now we note the tendency for Π_{ij} and ϕ_{ij} to diverge as $y_w \to 0$ (compare the chain-dot lines and the solid symbols in Figs. 4(b) and 5(b)), and for the pressure–strain and pressure–diffusion terms to reach large non-zero values of equal and opposite sign at the wall.) The net near-wall $-\overline{u'v'}$ decrease observed in Fig. 3(e) is accompanied by large decreases in both mean-shear production $-P_{12}^S = \overline{v'v'}\,\partial\bar{u}/\partial y$ and $-\Pi_{12}$, with the production falling slightly more rapidly, leading to a negative imbalance (see upper expanded-scale subplot in Fig. 4(a)). The net positive $-\partial\overline{u'v'}/\partial t$ in the outer layer is also due to a slightly more rapid change in $-P_{12}^S$. Notice that this is an indirect or 'extra-strain' effect, since the production $-P_{12}^A$ associated with the applied strain

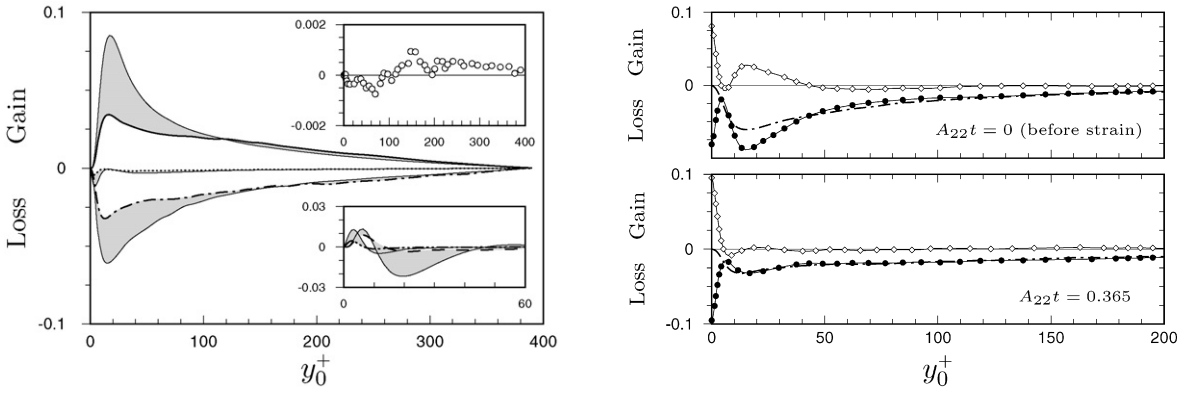

(a) (b)

Fig. 4. Terms in $-\overline{u'v'}$ Reynolds-shear stress budget from DNS of APG-strained channel [3] at $A_{22}t = 0.365$: —, $-P_{12}^S$; ···, $+\varepsilon_{12}$; –·–, $-\Pi_{12} = -\phi_{12} - \psi_{12}$ (also for $A_{22}t = 0$ in (b)); •, $-\phi_{12}$ (in (b) only); ◇, $-\psi_{12}$ (in (b) only); - - -, $-D_{12}^T$; –···–, $-D_{12}^\nu$; ○, sum of all terms ($\approx -\partial\overline{u'v'}/\partial t$) at $A_{22}t = 0.365$. Terms defined in Eq. (3.2). Thin-solid lines in (a) denote terms at $t = 0$ (before strain); shaded regions indicate change from unstrained initial conditions. Budget terms normalized by U_{ref}^4/ν, where $U_{\text{ref}} = 1.022\,u_\tau(0)$. Wall-normal coordinate $y_0^+ = y_w \exp(-A_{22}t)u_\tau(0)/\nu$. Results from [3].

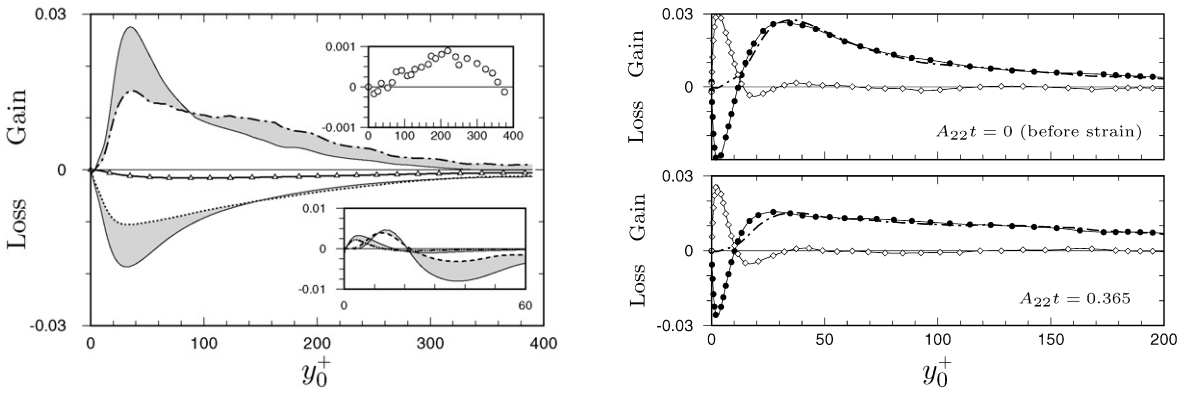

(a) (b)

Fig. 5. Terms in $\overline{v'v'}$ Reynolds normal-stress budget from DNS of APG-strained channel [3] at $A_{22}t = 0.365$: ···, $-\varepsilon_{22}$; –·–, $\Pi_{22} = \phi_{12} + \psi_{22}$ (also for $A_{22}t = 0$ in (b)); •, ϕ_{22} (in (b) only); ◇, ψ_{22} (in (b) only); - - -, D_{22}^T; –···–, D_{22}^ν; △, $P_{22}^A = -2\,\overline{v'v'}A_{22}$; ○, sum of all terms ($\approx \partial\overline{v'v'}/\partial t$) at $A_{22}t = 0.365$. Thin-solid lines in (a) denote terms at $t = 0$ (before strain); shaded regions indicate change from unstrained initial conditions. Normalization, symbols as in Fig. 4. Results from [3].

$A_{11} = -A_{22}$ is zero for this component. This again points to the non-trivial task faced by models applied to this flow.

We conclude this overview by turning to the equations describing the evolution of turbulence statistics, to be solved by the model-test code described below. The governing transport equations are most straightforward when written in terms of the new independent variables η and λ, where $\eta(y,t) = \exp(-A_{22}t)y = b(t)y$ and $\lambda(y,t) = t$. These 'deforming' coordinates (see [8,9,3,2]) allow the material derivative $\mathcal{D}(\,)/\mathcal{D}t$ to be replaced by the local temporal derivative $\partial(\,)/\partial\lambda$ in all transport equations, so that the equation for the mean streamwise velocity in the channel, $\bar{u}(\eta,\lambda)$, reduces to

$$\frac{\partial\bar{u}}{\partial\lambda} = -A_{11}\bar{u} + b(\lambda)\frac{\partial}{\partial\eta}\left[\nu b(\lambda)\frac{\partial\bar{u}}{\partial\eta} - \overline{u'v'}\right], \tag{2.2}$$

subject to the boundary condition $\bar{u} = U_w$ at $\eta = \pm h(0)$. (The $\overline{u_i' u_j'}$-transport equation in η, λ coordinates is given in (A.1a) of Appendix A.) The time-dependent wall velocity $U_w(\lambda)$ is defined by

$$U_w(\lambda) = U_c(\lambda) - U_c(0)\exp(A_{11}\lambda), \tag{2.3}$$

where $U_c(\lambda)$ and $U_c(0)$ are the mean centerline velocities at respectively the current time λ and that at which the strain was applied. The wall velocity must thus be dynamically adjusted in response to the current value of the time-dependent mean centerline velocity $U_c(\lambda)$, which is itself affected by the strain.[2] The evolution of U_c and U_w induced by the APG strain in the DNS is shown in Fig. 2. When viewed in a reference frame attached to the moving walls, the centerline velocity is given by $U_c(\lambda) = U_c(0)\exp(A_{11}\lambda)$, which provides the desired APG bulk deceleration. The $A_{22} > 0$ divergence will also cause the channel half-width h to increase with time as $h(\lambda) = h(0)\exp(A_{22}t)$. Note that in the deforming coordinates the location of the walls remains fixed at $\eta = \pm h(0)$.

3. Second-order models and model-test code

For incompressible flows the Reynolds-stress transport equation can be written:

$$\frac{\mathcal{D}\overline{u_i' u_j'}}{\mathcal{D}t} = P_{ij} + D_{ij}^{v} + D_{ij}^{T} + \Pi_{ij} - \varepsilon_{ij}, \tag{3.1}$$

where $\mathcal{D}\overline{u_i' u_j'}/\mathcal{D}t = \partial\overline{u_i' u_j'}/\partial t + \bar{u}_\ell \partial\overline{u_i' u_j'}/\partial x_\ell$ represents the mean-flow material derivative of $\overline{u_i' u_j'}$ and the right-hand side terms are:

$$\text{Production:} \quad P_{ij} = -\left(\overline{u_i' u_k'}\frac{\partial \bar{u}_j}{\partial x_k} + \overline{u_j' u_k'}\frac{\partial \bar{u}_i}{\partial x_k}\right),$$

$$\text{Viscous diffusion:} \quad D_{ij}^{v} = \frac{\partial}{\partial x_k}\left(\nu\frac{\partial\overline{u_i' u_j'}}{\partial x_k}\right),$$

$$\text{Turbulent transport:} \quad D_{ij}^{T} = -\frac{\partial}{\partial x_k}\left(\overline{u_i' u_j' u_k'}\right),$$

$$\text{Dissipation:} \quad -\varepsilon_{ij} = -2\nu\overline{\frac{\partial u_i'}{\partial x_k}\frac{\partial u_j'}{\partial x_k}}, \quad \text{and}$$

$$\text{Velocity–pressure-gradient correlation:} \quad \Pi_{ij} = -\left(\overline{\frac{u_i'}{\rho}\frac{\partial p'}{\partial x_j}} + \overline{\frac{u_j'}{\rho}\frac{\partial p'}{\partial x_i}}\right). \tag{3.2}$$

In order to distinguish between the direct effects of the irrotational applied strain A_{ij} and those arising indirectly through changes to the rotational mean $\bar{u}(y,t)$, the total rate of production P_{ij} is decomposed into its rotational (shear) and irrotational (applied-strain) components, $P_{ij} = P_{ij}^{S} + P_{ij}^{A}$ respectively, where

$$P_{ij}^{S} = -\overline{u_i' v'}\frac{\partial \bar{u}_j}{\partial y} - \overline{u_j' v'}\frac{\partial \bar{u}_i}{\partial y}, \tag{3.3a}$$

$$P_{ij}^{A} = -\overline{u_i' u_k'}A_{jk} - \overline{u_j' u_k'}A_{ik}. \tag{3.3b}$$

While the convection, production and molecular diffusion terms introduce no new unknowns, the turbulent transport D_{ij}^{T}, dissipation ε_{ij}, and velocity–pressure-gradient Π_{ij} tensors must be modeled. As mentioned in Section 2, the latter is often decomposed into pressure-transport ψ_{ij} and the pressure–strain ϕ_{ij} components:

$$\Pi_{ij} = \psi_{ij} + \phi_{ij}, \tag{3.4a}$$

with

$$\psi_{ij} = -\frac{\partial}{\partial x_k}\left(\frac{\overline{p' u_i'}}{\rho}\delta_{jk} + \frac{\overline{p' u_j'}}{\rho}\delta_{ik}\right) \quad \text{and} \quad \phi_{ij} = \overline{\frac{p'}{\rho}\left(\frac{\partial u_i'}{\partial x_j} + \frac{\partial u_j'}{\partial x_i}\right)}. \tag{3.4b}$$

[2] In both the DNS and model-test code, the centerline values from the previous time step are used to prescribe the wall velocities needed for the current time step.

While this decomposition is popular (largely because of the well-defined role of ϕ_{ij}, which acts solely to transfer energy between the three normal stresses), it is not unique [10,11] – and, as we shall see below, not optimal for wall-bounded flows. This has profound modeling implications, given the importance of the velocity–pressure-gradient correlation in determining the structure of the Reynolds-stress tensor. In 3D boundary layers, for example, Π_{23} tends to counteract the spanwise production term and is thus responsible for the unexpectedly slow growth of the spanwise Reynolds shear stress, and the resulting lack of agreement between the directions of the mean rate-of-strain and Reynolds-stress tensors [2]. The tendency for APG-strain-induced changes to the $-P_{12}^S$ shear production to be mirrored by a corresponding change to $-\Pi_{12}$ has already been observed (cf. Fig. 4). The importance of Π_{ij}, and the difficulty associated with modeling it correctly, is also implied by the wide variety of Π_{ij} (or ϕ_{ij}) models available. The behavior of this term will thus be a primary focus of this study.

3.1. Models tested

The Stress-transport closures tested here are by Launder and Shima [12], So et al. [13] and Wilcox [14]. (The first two will be denoted by the abbreviations LS and SAYS, respectively, the latter by Stress-ω.) LS and Stress-ω both employ the pressure–strain/pressure-transport decomposition for Π_{ij}, and use ϕ_{ij} models that are linear in the stress tensor $\tau_{ij} = \overline{u_i' u_j'}$. The LS pressure–strain model also makes explicit use of a wall-reflection term. By working with ϕ_{ij} rather than Π_{ij}, LS and Stress-ω implicitly include the pressure-transport term ψ_{ij} in their models for the turbulent transport D_{ij}^T. SAYS, on the other hand, assumes a weakly non-linear model (based on the SSG model [15]) for Π_{ij}, without recourse to the $\phi_{ij} + \psi_{ij}$ splitting, and models D_{ij}^T separately. For the third and final unknown, the LS and SAYS schemes solve a transport equation for the rate of turbulence energy dissipation ε whereas Wilcox's model solves for the specific dissipation rate ω. All closures were developed to be integrated through the viscous sublayer to the wall.

The choice to test these particular models was based on a desire to investigate the different approaches (linear versus non-linear pressure–strain model, the use of ϕ_{ij} versus Π_{ij}, and solving for ω instead of ε). A summary of each model follows. The form each takes when applied to the current strained-channel geometry is given in Appendix A.

3.1.1. Launder–Shima (LS) closure [12]

The high-Reynolds number version of this closure is based on the stress-transport model of Gibson and Launder [16]. Daly and Harlow's model [17] for the turbulent- and pressure-transport terms is used, with

$$D_{ij}^T + \psi_{ij} = \frac{\partial}{\partial x_k}\left(C_s \frac{k}{\varepsilon} \overline{u_k' u_\ell'} \frac{\partial \overline{u_i' u_j'}}{\partial x_\ell} \right), \tag{3.5}$$

where $k = \frac{1}{2}\overline{u_i' u_i'}$. LS [12] claim that this choice was made more for computational convenience rather than accuracy; they assumed that any errors are unlikely to have a significant effect due to the relative unimportance of the diffusive transport in the stress budgets for wall-bounded flows. (The validity of this assumption is examined below.) The dissipation tensor model makes the Kolmogorov assumption of local isotropy [18]:

$$\varepsilon_{ij} = \frac{2}{3}\varepsilon \delta_{ij}. \tag{3.6}$$

The pressure–strain model includes contributions from four terms, associated with the modification of the local pressure fluctuations by both mean (ϕ_{ij}^R) and turbulent (ϕ_{ij}^S) strains, and with wall-echo effects ($\phi_{ij\,W}^S + \phi_{ij\,W}^R$) that arise from the reflection of pressure fluctuations from the rigid wall, i.e.:

$$\phi_{ij} = \phi_{ij}^S + \phi_{ij}^R + \phi_{ij\,W}^S + \phi_{ij\,W}^R. \tag{3.7}$$

The slow-pressure–strain term is modeled according to Rotta's proposal,

$$\phi_{ij}^S = -2c_1 \varepsilon b_{ij}, \tag{3.8}$$

where

$$b_{ij} = \left(\overline{u_i' u_j'} - \frac{2}{3} k \delta_{ij} \right) \Big/ k$$

is the Reynolds-stress anisotropy tensor. The rapid component is given by

$$\phi_{ij}^R = -c_2\left(P_{ij} - \frac{2}{3}\delta_{ij}\mathcal{P}\right), \tag{3.9}$$

where $\mathcal{P} = \frac{1}{2}P_{kk}$. The wall-reflection terms are:

$$\begin{aligned}\phi_{ij\,W}^S &= c_1^w \frac{\varepsilon}{k}\left(\overline{u'_k u'_m} n_k n_m \delta_{ij} - \frac{3}{2}\overline{u'_k u'_i} n_k n_j - \frac{3}{2}\overline{u'_k u'_j} n_k n_i\right) f,\\ \phi_{ij\,W}^R &= c_2^w\left(\phi_{km}^R n_k n_m \delta_{ij} - \frac{3}{2}\phi_{ik}^R n_k n_j - \frac{3}{2}\phi_{jk}^R n_k n_i\right) f,\end{aligned} \tag{3.10}$$

where f is a near-wall damping function and n_i the wall-normal unit vector. Because of the parallel-flow geometry considered here, the wall-reflection terms are especially straightforward, since the unit vector reduces to $n_i = \delta_{i2}$ for both the unstrained and strained cases. (The presence of the unit-normal vectors in (3.10) represents a practical disadvantage when this scheme is applied to more complicated geometries.) The quantities C_s, c_1, c_2, c_1^w and c_2^w are all model coefficients, some of which are constant (see Appendix A). Eq. (3.10) is designed to redistribute the energy in velocity fluctuations in the direction normal to the wall to those parallel to it [12]. In order to extend the closure to the viscous sublayer, LS implement the suggestion of Lumley [19,20] and changed only the pressure–strain term. The effect of the departure from local isotropy of the dissipation tensor in the vicinity of the surface is accounted for in the near-wall correction to ϕ_{ij}. Eq. (3.5) is retained without modification on the assumption that the turbulent transport has relatively little influence. The near-wall modification to ϕ_{ij} is accomplished through altering the coefficients c_1, c_2, c_1^w and c_2^w (see Appendix A) so that as the wall is approached, the two-component limit of turbulence is recovered. The form of the near-wall modifications was chosen so that for high-Reynolds number simple shear flows, the constants proposed by Gibson and Launder are obtained [16]. Another constraint was to reproduce the expected variation of the Reynolds stresses in the buffer region of the flat-plate boundary layer.

LS uses an ε-transport equation with special terms added to address problems relating to insufficient ε in flows approaching separation, and to prevent spurious relaminarization. Further details can be found in [12] and, for the case of the APG-strained channel, in Appendix A.

3.1.2. So et al. (SAYS) closure [13]

The objective of So et al. [13] was to develop a second-order closure to capture near-wall ('low-Reynolds-number') effects in the calculations of two-dimensional, wall-bounded flows. Hanjalic and Launder's [21] model is used for turbulent transport, such that

$$D_{ij}^T = \frac{\partial}{\partial x_k}\left[C_s \frac{k}{\varepsilon}\left(\overline{u'_i u'_\ell}\frac{\partial \overline{u'_j u'_k}}{\partial x_\ell} + \overline{u'_j u'_\ell}\frac{\partial \overline{u'_k u'_i}}{\partial x_\ell} + \overline{u'_k u'_\ell}\frac{\partial \overline{u'_i u'_j}}{\partial x_\ell}\right)\right]. \tag{3.11}$$

Eq. (3.11) is applied throughout the entire flow without being modified for use in regions close to solid boundaries, on the assumption that D_{ij}^T is of higher order than the dissipation tensor ε_{ij} and the velocity–pressure-gradient correlation Π_{ij}, both of which were thought to be more important near solid walls. The model for the dissipation tensor is

$$\varepsilon_{ij} = \frac{2}{3}\varepsilon\delta_{ij} + f_{w1}\frac{\varepsilon}{k}\left[-\frac{2}{3}k\delta_{ij} + \frac{\overline{u'_i u'_j} + \overline{u'_i u'_k} n_k n_j + \overline{u'_j u'_k} n_k n_i + n_i n_j \overline{u'_k u'_\ell} n_k n_\ell}{1 + \frac{3}{2}\overline{u'_m u'_p} n_m n_p / k}\right]. \tag{3.12}$$

This was postulated by Lai and So [22]. The damping function f_{w1} is based on the turbulent Reynolds number, $Re_t = k^2/\varepsilon\nu$. At high Reynolds number, the ε_{ij} model contracts, as required, to Kolmogorov's isotropic result, Eq. (3.6). Following Launder and Reynolds [23], Eq. (3.12) asymptotes to the correct $y_w \to 0$ limit for each component of the $\varepsilon_{\alpha\beta}/\overline{u'_\alpha u'_\beta}$ ratio, $(\alpha, \beta) = 1, 2, 3$ (no sum on repeating indices).

The velocity–pressure-gradient model is based on the high-Reynolds number pressure–strain closure of Speziale et al. [15]; the extension to the viscous sublayer consists of introducing a pressure-transport model ψ_{ij} and a near-wall correction tensor $\phi_{ij\,W}$, with the aim of achieving asymptotic consistency of the Reynolds-stress equations as a solid boundary is approached (away from the wall, there is assumed to be no difference between Π_{ij} and ϕ_{ij}). The

damping function f_{w1} is included in $\phi_{ij\,W}$ in order to diminish the latter's influence further away from the wall. The full velocity–pressure-gradient model is:

$$\Pi_{ij} = -\big(C_1\varepsilon + C_1^*\mathcal{P}\big)b_{ij} + C_2\varepsilon\left(b_{ik}b_{kj} - \frac{1}{3}\Pi\delta_{ij}\right) - \alpha_1\left(P_{ij} - \frac{2}{3}\mathcal{P}\delta_{ij}\right) - \beta_1\left(D_{ij} - \frac{2}{3}\mathcal{P}\delta_{ij}\right) - 2\left(\gamma_1 + \frac{1}{2}C_3^*\Pi^{1/2}\right)kS_{ij} + \phi_{ij}^W + \psi_{ij}, \tag{3.13}$$

where $D_{ij} = -\overline{u_i'u_k'}\,\partial\bar{u}_k/\partial x_j - \overline{u_j'u_k'}\,\partial\bar{u}_k/\partial x_i$, with

$$\phi_{ij}^W = f_{w1}\left[\big(C_1\varepsilon + C_1^*\mathcal{P}\big)b_{ij} - C_2\varepsilon\left(b_{ik}b_{kj} - \frac{1}{3}\Pi\delta_{ij}\right) + \alpha^*\left(P_{ij} - \frac{2}{3}\mathcal{P}\delta_{ij}\right) + 2\gamma^*kS_{ij}\right], \tag{3.14a}$$

and

$$\psi_{ij} = -\frac{1}{3}\left[\frac{\partial}{\partial x_\ell}\left(\nu\frac{\partial\overline{u_i'u_k'}}{\partial x_\ell}\right)n_kn_j + \frac{\partial}{\partial x_\ell}\left(\nu\frac{\partial\overline{u_j'u_k'}}{\partial x_\ell}\right)n_kn_i\right] + \frac{1}{3}\frac{\partial}{\partial x_m}\left(\nu\frac{\partial\overline{u_k'u_\ell'}}{\partial x_m}\right)n_kn_\ell n_in_j. \tag{3.14b}$$

The parameters C_s, C_1, C_1^*, C_2, C_3^*, α_1, β_1, γ_1, α^* and γ^* are all model constants, while $\Pi = b_{ij}b_{ij}$ is a measure of the Reynolds-stress anisotropy, S_{ij} is the mean strain-rate tensor and D_{ij} is a variation of the production tensor P_{ij} (see Appendix A). The rationale for the choice of the constants in the damping function and near-wall correction tensor is given in [13]. The SAYS dissipation equation includes a new right-hand-side term to account for near-wall effects (see Appendix A).

A generalization of the SAYS closure has also been proposed by Yuan and So [24], which avoids use of wall-unit-normals in the ε_{ij} and ψ_{ij} models, in order to remove the awkwardness associated with application of SAYS to complex-geometry flows. However, in light of the simplicity of the parallel-flow strained-channel geometry, we have chosen to implement and test the original (presumably more accurate) closure.

3.1.3. Wilcox Stress-ω closure [14]

This scheme was designed as a generalization of its author's two-equation k–ω model, and therefore, in contrast to LS and SAYS, employs a transport equation for the rate of specific dissipation $\omega \sim \varepsilon/k$ rather than for ε itself. The turbulent transport and pressure transport are together modeled by a gradient-diffusion hypothesis, with

$$D_{ij}^T + \psi_{ij} = \frac{\partial}{\partial x_k}\left(\sigma^*\nu_T\frac{\partial\overline{u_i'u_j'}}{\partial x_k}\right), \tag{3.15}$$

where σ^* is a constant turbulent Prandtl number and $\nu_T \sim k/\omega$ the scalar eddy viscosity (see Appendix A). The dissipation tensor is assumed to be purely isotropic,

$$\varepsilon_{ij} = \frac{2}{3}\beta^*\omega k\delta_{ij}, \tag{3.16}$$

where β^* is a scalar function of k and ω. Stress-ω uses a linear Launder–Reece and Rodi pressure–strain model, with the slow pressure–strain term replaced by the Rotta expression (3.8), and the rapid component given by:

$$\phi_{ij}^R = -\hat{\alpha}\left(P_{ij} - \frac{2}{3}\mathcal{P}\delta_{ij}\right) - \hat{\beta}\left(D_{ij} - \frac{2}{3}\mathcal{P}\delta_{ij}\right) - \hat{\gamma}kS_{ij}, \tag{3.17}$$

where the production and strain terms have their usual meaning, defined above. No wall-reflection terms are included in the pressure–strain model. In the high-Reynolds number version, the values for $\hat{\alpha}$, $\hat{\beta}$ and $\hat{\gamma}$ are those suggested by Launder et al. [25]. These depend on a constant (C_2, see Appendix A) that Wilcox sets to optimize sublayer predictions. Low-Reynolds number (i.e. near-wall) corrections involve replacing $\hat{\alpha}$, $\hat{\beta}$, $\hat{\gamma}$ and the other closure coefficients by viscous damping functions that are similar to those used by the k–ω model. Definitions of all terms and parameters are presented in Appendix A, as applied to the strained channel; the general form is given in [14].

3.2. Strained-channel model-test code

Solutions of the model equations were obtained using the finite-difference code described in [1], which was itself a modified version of the code ('Pipe.f') originally developed by Wilcox [14] for solving steady-state unstrained plane-channel flow.

Both the original and strained-channel codes use a second-order Crank–Nicolson discretization (in y and η respectively). Symmetry is invoked so that the transport equations are solved over the lower-half-channel domain. At the centerline, $y_w = h(t)$, zero first derivatives are imposed as boundary conditions for the mean streamwise and spanwise velocities, $(\partial\bar{u}/\partial y)_c = (\partial\bar{w}/\partial y)_c = 0$. (A second-order implementation of this Neumann condition is required to keep precise control of the $U_c - U_w$ history.) The corresponding boundary conditions for the other turbulent statistics involved in the solutions are given in Appendix A. The transport equations are integrated through the viscous sublayer with no-slip boundary conditions assumed. To ensure spatial accuracy, 400 grid points between the wall and channel centerline were utilized, with the first point at 0.15 initial wall units $y_0^+ = \eta_w u_\tau(0)/\nu = y_w \exp(-A_{22}t)u_\tau(0)/\nu$ away from the wall (the zero subscript on y_0^+ indicates that the deforming coordinate is normalized by wall units from the unstrained-plane-channel initial condition, rather than from the current time). A geometric grid stretching monotonically clusters the grid points near the wall, such that 120 points are located between the wall and $y_0^+ = 30$. The same spatial discretization was used for all three models in every case. We also briefly consider the effect of using a grid with only 28 points across the half-channel, such that the first point off the wall is at $y_0^+ = 0.5$ and only 15 points fall between the wall and $y_0^+ = 30$, in order to determine the sensitivity of the models to the use of resolution typical of industrial-flow applications. A fixed time step Δt of 1.25×10^{-2} initial wall time units was found to be sufficiently small for all but the SAYS runs, which (presumably due to its increased numerical stiffness) required a time step of 1.25×10^{-3}, to ensure grid-independent results.

4. Results

4.1. Unstrained plane-channel predictions

Before considering straining effects, the models will be applied to unstrained plane-channel flow and compared to the 'precursor' DNS used to obtain the strained-channel initial conditions in [3]. First- and second-order statistics and individual source/sink/transport terms computed by the initial-condition model-test code are compared to the pre-strained DNS data at $Re_\tau = 390$. The same exercise has been performed for $Re_\tau = 180$ by both Wilcox [14] for his Stress-ω model, and by Sciberras [26] for all three models tested here. This will provide a context for each model's behavior for the strained flow.

Fig. 6 presents the mean velocities in both inner- and outer-layer scaling. Also included in Fig. 6(a) is the result of using the Spalart–Allmaras (SA) one-equation model (open symbols), which of the four schemes tested in [1] (the other candidates were the Baldwin–Lomax algebraic and the Launder–Sharma and Menter SST two-equation models) gave the closest agreement with the mean velocity in the inner-layer scaling. (Note that since u_τ is imposed for each model, given that Re_τ is an input parameter, the very-near-wall velocity in the inner-layer scaling for each model must match the DNS.) The Stress-ω predictions best agree with the DNS when the velocities are normalized by inner-layer variables, and the entire wall-to-centerline region is considered. It is noteworthy, however, that for this quantity, SA captures the inner-layer behavior at least as well as Stress-ω, and certainly much better than LS and SAYS. For Stress-ω, the good performance can be traced to the fact that the constant C_2 in its pressure–strain model was tuned to optimize sublayer predictions to yield a satisfactory value for the additive constant in the law of the wall (and this without recourse to low-Reynolds-number corrections [14]). The LS inner-layer profile, on the other hand, deviates from the DNS result from deep within the inner-layer. The non-standard (too small) effective von Karman constant yielded by this closure was also observed in [27]. The SAYS velocity also differs from the DNS, but not by as much as it does for LS. At $Re_\tau = 180$, however, Sciberras [26] found the LS and SAYS predictions to be essentially equivalent, in both inner and outer scalings. This Reynolds-number sensitivity is a warning not to over-generalize findings based on DNS at a single Reynolds number, especially when it is very low. In the outer-layer scaling, with $\bar{u}$ normalized by the mean centerline velocity U_c, the LS result is marginally best above $y_w = 0.1h$; nearer the surface Stress-ω is again closest to the DNS (Fig. 6(b)).

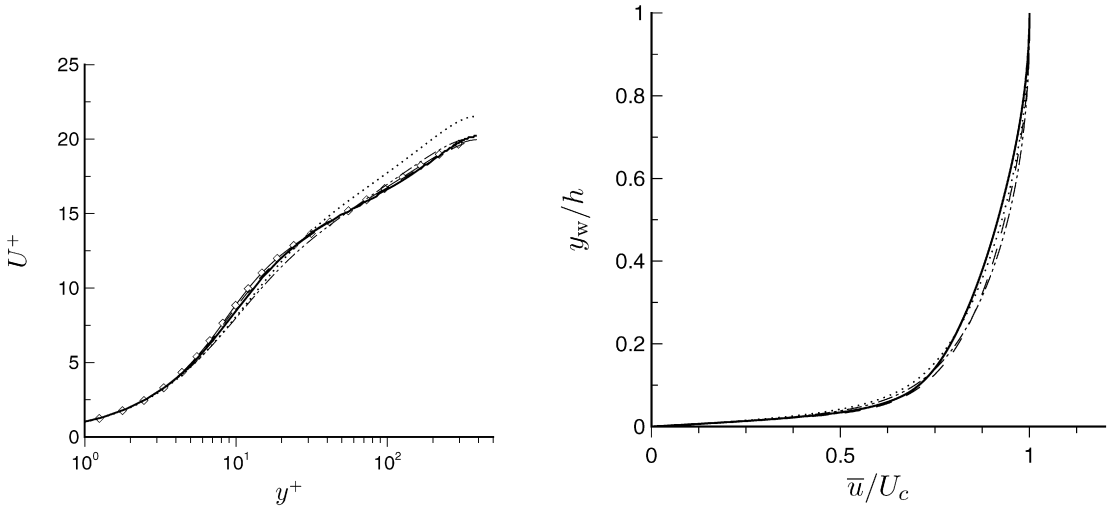

(a) (b)

Fig. 6. DNS and model predictions of mean velocity in (a) inner-layer and (b) outer-layer scaling for unstrained plane-channel flow at $Re_\tau = 390$: —, DNS; - - -, Stress-ω; ···, LS; –·–, SAYS; ⋄, Spalart–Allmaras (from [1]). Velocities measured with respect to coordinate system attached to streamwise moving walls (cf. Fig. 2). Distance to the nearest wall $y_w = |y| - h$.

Table 1
DNS and model predictions of skin friction $C_f = 2u_\tau^2/U_m^2$ for unstrained plane-channel flow at $Re_\tau = 390$

Case	U_c/u_τ	$C_f \times 10^3$
DNS	20.20	6.47
SA	19.95	6.45
SST	19.43	6.72
LS	21.51	5.71
SAYS	20.10	6.35
Stress-ω	19.82	6.51

Large variations in the predictions of the Reynolds shear stress $-\overline{u'v'}$ are not expected, since in the absence of the A_{ij} straining, *any* steady-state plane-channel solution will produce a linear outer-layer profile (provided the viscous stress is appropriately small). Differences are solely in the maximum $-\overline{u'v'}$ and the location at which it occurs. LS and SAYS both underestimate the maximum, although their prediction of its location is fairly close to the DNS, while the magnitude and location of $-\overline{u'v'}_{\max}$ given by the Stress-ω model are both close to the DNS results (not shown; see [28]). Table 1 summarizes the skin friction coefficient $C_f = \tau_w/(\frac{1}{2}\rho U_m^2)$ given by the DNS and the models, where C_f is defined in terms of U_m, the bulk (mixed-mean) average velocity. Results from the Spalart–Allmaras (SA) and Menter SST models, tested in [1], are also included, for comparison. The good agreement between Stress-ω and the DNS for the U^+ profiles implies that the C_f predicted by the Stress-ω model will also be close to the DNS. The discrepancy is only 0.6% (although SA is even closer, within 0.3% of the DNS). The SST C_f is 4% higher than the DNS, while the SAYS and LS values are respectively 2% and 12% lower. (Since the ratio $U_m/U_c = 0.87$ estimated by LS is the same as that given by the DNS, the discrepancy remains when C_f is defined using the centerline velocity U_c.) Such a large underestimation of the skin friction is a consequence of the too-high U_c/u_τ predicted by LS, illustrated in Fig. 6(a).

The ratio of the rates of turbulence kinetic energy production $\mathcal{P} = \frac{1}{2}P_{ii}$ to dissipation $\varepsilon = \frac{1}{2}\varepsilon_{ii}$ given by the models and the DNS is presented in Fig. 7, along with the corresponding ε profiles for the DNS and the two models that explicitly use it. The DNS profile of $\mathcal{P}/\varepsilon$ is typical of other plane-channel simulations, both in terms of the value of the near-wall peak as well as the tendency for $\mathcal{P}$ to begin slightly less than ε near $y^+ = 60$ and increase monotonically

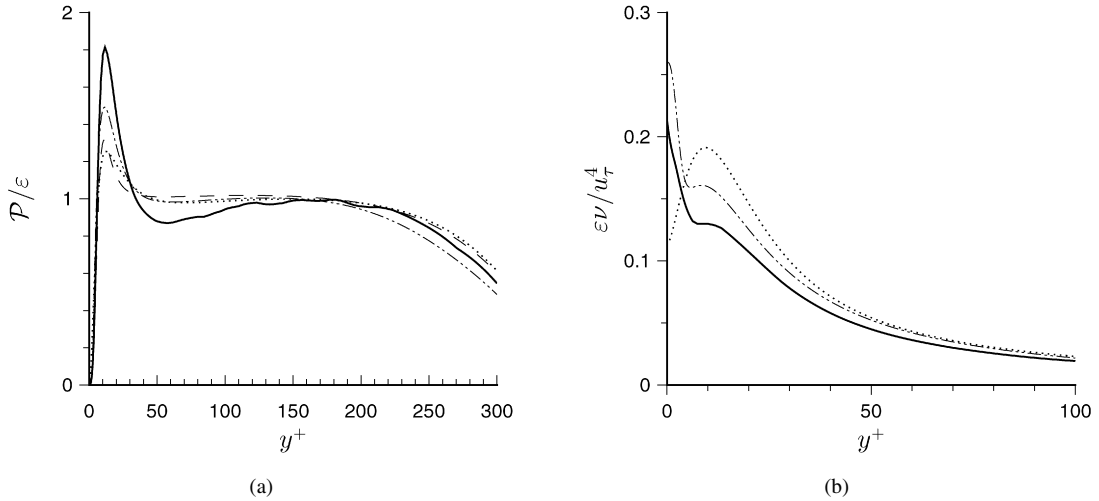

Fig. 7. DNS and model predictions of (a) production-to-dissipation ratio $\mathcal{P}/\varepsilon$ and (b) dissipation ε for unstrained plane-channel flow at $Re_\tau = 390$: —, DNS; - - -, Stress-ω; ⋯, LS; –·–, SAYS.

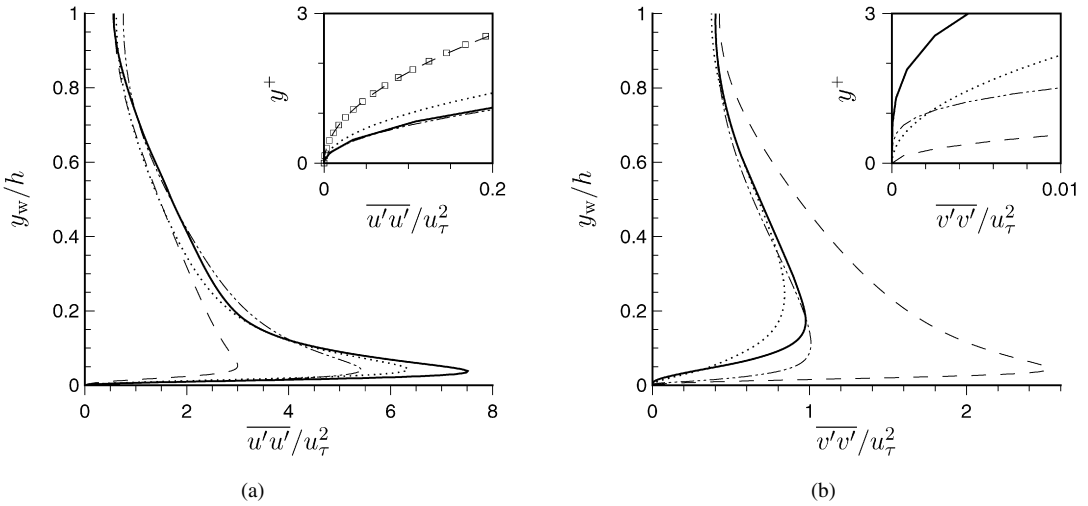

Fig. 8. DNS and model predictions of (a) $\overline{u'u'}$ and (b) $\overline{v'v'}$ Reynolds normal stresses for unstrained plane-channel flow at $Re_\tau = 390$: —, DNS; - - -, Stress-ω; ⋯, LS; –·–, SAYS; □, Stress-ω $\overline{v'v'}$ (in subplot in (a) only).

with y^+ towards $\mathcal{P}/\varepsilon = 1$ throughout the logarithmic region [29]. Fig. 7(a) indicates that all three models come closer to the $\mathcal{P} = \varepsilon$ log-layer idealization than the DNS does.

A serious shortcoming of Stress-ω is revealed in Fig. 8, which presents profiles of streamwise $\overline{u'u'}$ and wall-normal $\overline{v'v'}$ normal stresses. Stress-ω significantly under- and over-predicts $\overline{u'u'}$ and $\overline{v'v'}$ respectively. The best that can be said for the Stress-ω results in Fig. 8 is that the y_w at which the maximum $\overline{u'u'}$ occurs is fairly close to that for the DNS (which is also true for the other two models). Given its good C_f and $\bar{u}$ predictions (and reasonable profiles of k (not shown) and $-\overline{u'v'}$ (Fig. 16(a) subplot)), the degree to which Stress-ω fails to account for the near-wall Reynolds-stress anisotropy was not expected. In fact $\overline{u'u'}$ and $\overline{v'v'}$ for Stress-ω are roughly equivalent across the channel, and their near-wall peak values only differ by about $0.5u_\tau^2$ (in contrast to the $6.5u_\tau^2$ peak difference for the DNS).

The nearly isotropic state of the Stress-ω stresses is quantified in Fig. 9, which presents components of the Reynolds-stress anisotropy tensor $b_{ij} = (\overline{u_i'u_j'} - \frac{2}{3}k\delta_{ij})/2k$ for all three models and the DNS. Each of the normal-stress components b_{11}, b_{22} and b_{33} for Stress-ω (dashed lines) are much closer to the $b_{ij} = 0$ isotropic limit than is the DNS or either of the other two models. Even in the $y_w \to 0$ limit, Stress-ω gives $\overline{u'u'}$ and $\overline{v'v'}$ profiles that are nearly

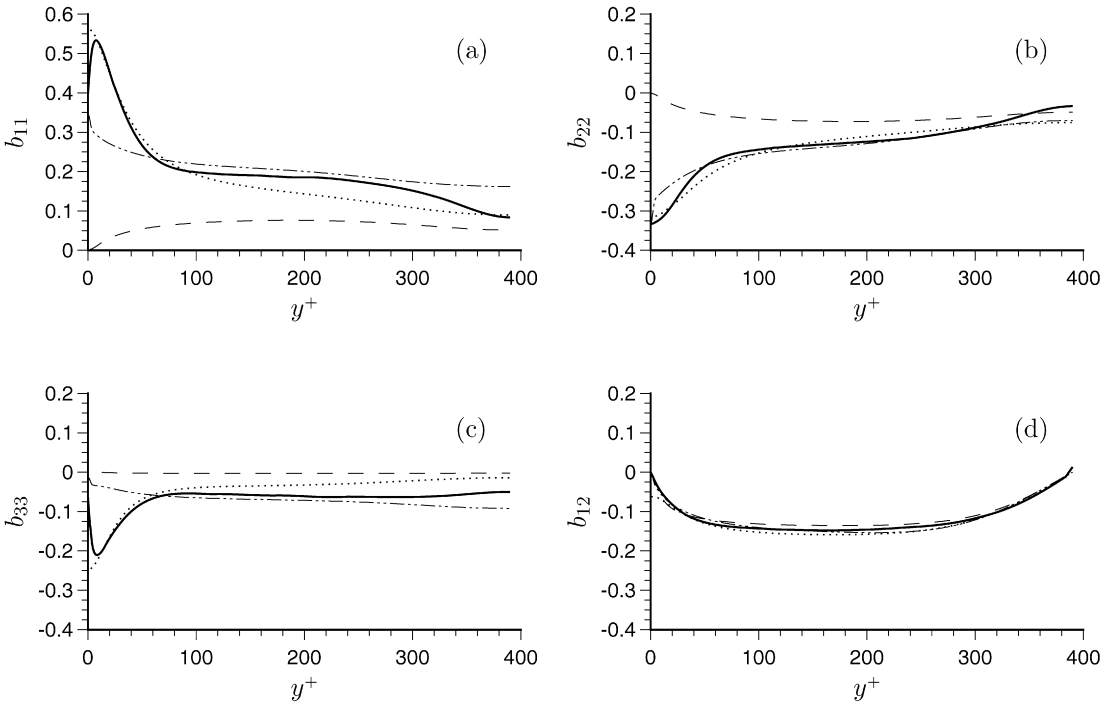

Fig. 9. DNS and model predictions of (a) b_{11}, (b) b_{22}, (c) b_{33} and (d) b_{12} components of Reynolds-stress anisotropy tensor $b_{ij} = \overline{u_i' u_j'}/2k - \frac{1}{3}\delta_{ij}$ for unstrained plane-channel flow at $Re_\tau = 390$: —, DNS; - - -, Stress-ω; ···, LS; —·—, SAYS.

coincident (compare the dashed line and open symbols in Fig. 8(a) subplot). The link between b_{ij} and a scheme's pressure–strain model is a strong one [11]. Demuren and Sarkar [30] have shown that in regions where transport is negligible, where the rate of dissipation is isotropic (such that $\varepsilon_{ij} \sim \varepsilon\delta_{ij}$) and where the rates of turbulence kinetic energy and dissipation are equivalent, each element of the pressure–strain/dissipation ratio ϕ_{ij}/ε depends only on the structure of the b_{ij} tensor. Consequently, within the log region, the relationship between each of the Reynolds-stress components is determined solely by the ϕ_{ij} model (and not for example by the details of the ε-transport equation). Fig. 9 results thus reflect poorly on the ϕ_{ij} model used by Stress-ω. (The performance of the Stress-ω ϕ_{ij} model will be revealed more explicitly below, when terms in each model's Reynolds-stress budget are compared to those from the DNS.) It is striking, however, that despite the poor representation of the normal-stress anisotropies, Stress-ω is able to capture the shear-stress anisotropy b_{12} as well as it does (Fig. 9(d)).

The $\overline{u'u'}$ and $\overline{v'v'}$ stresses given by LS (dotted lines) are in general closest to the DNS, especially near the wall. This is true both in terms of their anisotropies (Fig. 9) and magnitude (Fig. 8) – although LS does under-predict both $\overline{u'u'}$ and $\overline{v'v'}$ by about 15–20%. Nevertheless, the good overall agreement points to the general success of the LS wall-reflection term $\phi_{ij\,W}$ and/or low-Reynolds number modifications (cf. Section 3.1.1) in effecting the $\overline{v'v'}$ to $\overline{u'u'}$ energy transfer both very near the wall and within the logarithmic region. The behavior of the constituents of the LS pressure–strain model will be assessed in detail in the next section, for the flow subjected to the APG strain.

In an attempt to address asymptotic deficiencies in second-order statistics near the wall, So et al. [27] examined near-wall Taylor-series expansions given by a range of stress-transport closures. For LS, they found that the rate at which some of the Reynolds stresses approach $y_w = 0$ does not formally match the exact result [31]. The SAYS closure (whose development was informed by the So et al. study [27]), while not making explicit use of a wall-reflection term, introduces a near-wall correction $\phi_{ij\,W}$ (Section 3.1.2) to enforce consistency of $\overline{u_i' u_j'}$ as the wall is approached. Also, it is the only model tested here that explicitly accounts for pressure transport ψ_{ij}, rather than including it in the turbulence transport model. The SAYS Reynolds-stress scheme is asymptotically correct to at least order y_w, and for some components to order y_w^2 [13]. Very near the wall, the SAYS results best agree with the $\overline{v'v'}$ and especially the $\overline{u'u'}$ distribution given by the DNS (see subplots in Fig. 8). Unfortunately, the effect of this good agreement very near the wall does not extend much above it, since over most of the flow the $\overline{u'u'}$ and $\overline{v'v'}$ profiles by SAYS are no better,

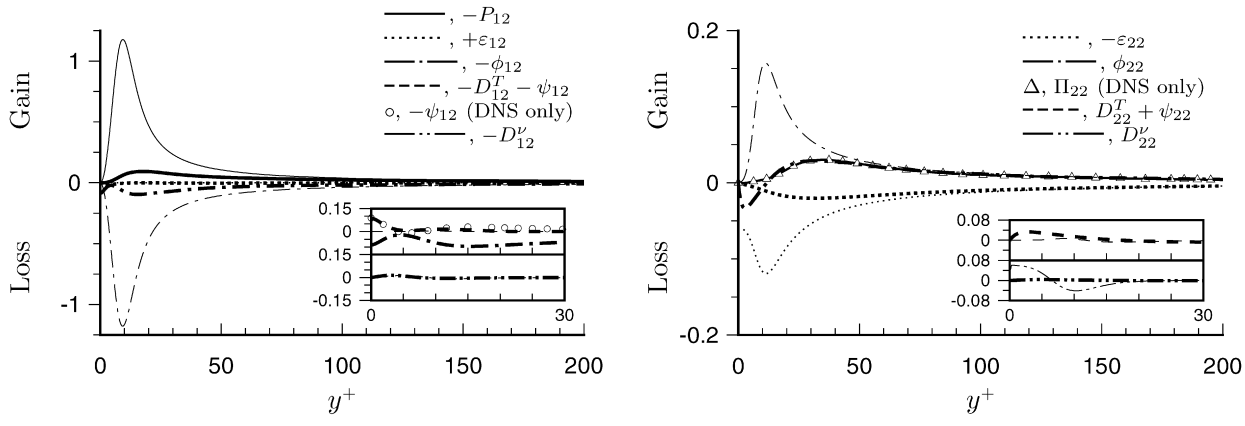

(a) Stress-ω $-\overline{u'v'}$ budget

(b) Stress-ω $\overline{v'v'}$ budget

Fig. 10. Terms in the Stress-ω budget of (a) $-\overline{u'v'}$ and (b) $\overline{v'v'}$ Reynolds stresses for unstrained-channel flow at $Re_\tau = 390$. DNS results shown as thicker version of model curves. (DNS and Stress-ω curves for ε_{12} and $-D_{12}^\nu$ are coincident in (a).) Budget terms normalized by u_τ^4/ν.

and in some regions worse, than those for LS. SAYS does however manage to reproduce some degree of anisotropy in the near-wall values of the normal stresses, and in fact in the logarithmic region its b_{11}, b_{22} and b_{33} are marginally better than that given by LS.

We now turn to an examination of the individual terms in the Reynolds-stress budgets associated with each closure. But before doing so a word of caution is perhaps in order. While we expect this to be an instructive exercise, and that differences between the terms given by the DNS and by the models will shed light on their strengths and weakness, ultimately it is the accuracy given by the overall *net effect* of a closure that matters. In fact, since the Reynolds-stress evolution is typically the result of small differences between much larger individual budget terms (see e.g. [2,3]), it is often wise to deliberately apply a model to the sum of two or more of the production, dissipation and/or transport terms (e.g. as was done implicitly for the dissipation and pressure–strain sum $\phi_{ij} - \varepsilon_{ij}$ by LS). Consequently, even a large difference between the actual individual budget term and a closure's representation of it is not in-and-of-itself a cause for concern, unless that difference can be related to an anomaly in the net prediction.

With this caution in mind, we begin in Fig. 10 with terms in the Stress-ω closure. (The DNS terms are represented in all budget figures as thicker-version lines of the corresponding RANS profiles.) One of the messages from the $-\overline{u'v'}$ budget (Fig. 10(a)) is the reasonableness of Stress-ω's neglect of the $-\overline{u'v'}$ component of the dissipation $-\varepsilon_{12}$, since for the DNS its magnitude is everywhere less than $0.013u_\tau^4/\nu$ (dotted lines). Fig. 10(a) also reveals the effect of using a single gradient-diffusion model to represent the sum of the turbulent-transport $-D_{12}^T$ and pressure-transport ψ_{12} terms (or equivalently, by representing the velocity–pressure-gradient correlation $-\Pi_{12}$ solely with a model for the pressure–strain term $-\phi_{12}$). The discrepancy is largest near the wall, as shown by the difference between the thin-dashed and thick-dashed lines in the Fig. 10(a) subplot, which respectively correspond to the $-D_{12}^T - \psi_{12}$ model and the sum from the DNS. The model does not capture the $y_w = 0$ maximum observed in the DNS of the turbulent-transport/pressure-transport sum, $-D_{12}^T - \psi_{12}$, which below $y^+ = 5$ is dominated by the $-\psi_{12}$ term (note the convergence as $y_w \to 0$ of the thick-dashed line ($-D_{23}^T - \psi_{12}$) and open-circle symbols ($-\psi_{12}$) in Fig. 10(a)). This underlines the conceptual advantage, pointed out for example by Mansour et al. [31] and Pope [11], of using Π_{ij} and D_{ij}^T, rather than ϕ_{ij} and $D_{ij}^T + \psi_{ij}$, when designing a second-order closure. In fact, Stress-ω implicitly does this, by using a Π_{ij} model for ϕ_{ij} and a gradient-diffusion model for $D_{ij}^T + \psi_{ij}$ that fails to capture ψ_{ij}. The neglect (or misrepresentation) of ψ_{ij} by Stress-ω is thus not *per se* a serious matter, at least for this flow.

However, Stress-ω does exhibit a much larger and potentially serious model-versus-DNS discrepancy in the $-\overline{u'v'}$ production and pressure–strain terms (main plot in Fig. 10(a)). The greatly exaggerated $-P_{12} = \overline{v'v'}\,\mathrm{d}\bar{u}/\mathrm{d}y$ is a consequence of the striking overprediction of the wall-normal Reynolds stress $\overline{v'v'}$. This in turn leads to the exaggerated $-\phi_{12}$, which must counteract $-P_{12}$ in order for Stress-ω to produce a reasonable $-\overline{u'v'}$ prediction. The P_{12}-versus-ϕ_{12} balance is effected almost entirely by the low-Reynolds-number correction to the $\hat{\alpha}$ term of the rapid component ϕ_{ij}^R (see Eq. (3.17)), such that $-\phi_{12} \approx \hat{\alpha} P_{12}$ over the bulk of the flow (and $|\hat{\alpha} P_{12}/\phi_{12}| = 0.97$ at the near-wall minimum

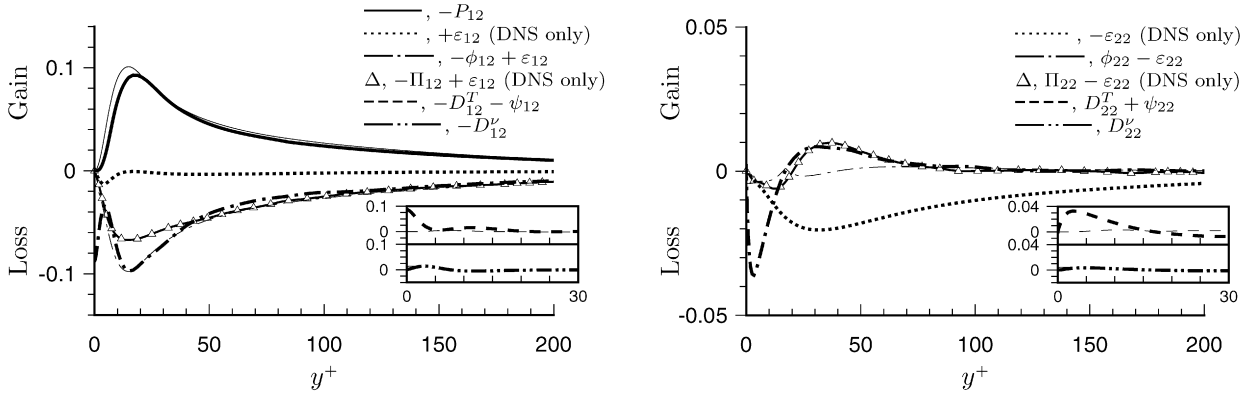

(a) LS $-\overline{u'v'}$ budget (b) LS $\overline{v'v'}$ budget

Fig. 11. Terms in the LS budget of (a) $-\overline{u'v'}$ and (b) $\overline{v'v'}$ Reynolds stresses for unstrained-channel flow at $Re_\tau = 390$. DNS results shown as thicker version of model curves. (DNS and LS curves for $-D^\nu_{12}$ and D^ν_{22} are coincident.) Normalization as in Fig. 10.

near $y^+ = 10$). The return-to-isotrophy component $-\phi^S_{12}$, in contrast, is negligible here, as are the other rapid-pressure ($\hat{\beta}$ and $\hat{\gamma}$) terms. That $\hat{\alpha}$ carries the near-wall behavior is reflected in the fact that the low-Reynolds-number corrections (see Appendix A) $\hat{\beta}/\hat{\beta}_\infty$ and $\hat{\gamma}/\hat{\gamma}_\infty$ both approach zero as $y^+ \to 0$, while $\hat{\alpha}/\hat{\alpha}_\infty$ is a maximum (≈ 1.29) at the wall.

Significant differences between the Stress-ω and DNS profiles are also apparent in the $\overline{v'v'}$ budget, shown in Fig. 10(b). The inability of Stress-ω to reproduce the near-wall departure from isotropy of ε_{22} (recall that Stress-ω invokes Kolmogorov's isotropy hypothesis for ε_{ij}) is responsible for the spurious viscous transport D^ν_{22} as $y_w \to 0$, needed to close the near-wall budget (Fig. 10(b)). The pressure–strain discrepancies are both quantitative and qualitative. For plane-channel flow the $\overline{v'v'}$ production P_{22} is zero, and the Stress-ω pressure–strain term acts purely as a source; the DNS shows that ϕ_{22} is actually both a source (in the outer layer) and a sink (near the wall). The velocity–pressure gradient Π_{22} on the other hand is everywhere a $\overline{v'v'}$ source (open triangles). The disadvantage of using ϕ_{ij} rather than Π_{ij} – and the consequence of including ψ_{ij} in the D^T_{ij} model – is again evident. For this stress, the $\hat{\alpha}$ term in the rapid-pressure strain model ϕ^R_{22} again controls the behavior of ϕ_{22}. (At the near-wall peak at $y^+ = 11$, $\hat{\alpha}\frac{2}{3}\mathcal{P} = 0.96\,\phi_{22}$.) The errant normal-stress anisotropies for Stress-ω are thus associated with the near-wall $\hat{\alpha}/\hat{\alpha}_\infty$ correction.

For the LS budgets, the pressure–strain and dissipation tensors are grouped together, since for this scheme the near-wall departure from isotropy of ε_{ij} is accounted for by the ϕ_{ij} model. We have already observed one point in favor of the ϕ_{ij} model itself, in the generally good agreement with the DNS of the anisotropy b_{ij} given by LS[3] (Fig. 9). The $-\overline{u'v'}$ budget given by the LS model is presented in Fig. 11(a). (Also included for reference are the ε_{ij} from the DNS.) The $-\phi_{12}+\varepsilon_{12}$ term is in good agreement with the DNS except very near the wall, for $y^+ < 5$, where it fails to capture the non-zero local minimum at the wall, associated with the pressure–strain term (see Fig. 4(b), and the open triangles in Fig. 11(a), denoting $-\Pi_{12}+\varepsilon_{12}$ from the DNS). (This is consistent with the b_{ij} results shown in Fig. 9, in that the LS and DNS profiles, especially of b_{11}, b_{33} and b_{12}, closely agree between $y^+ = 20$ and 100, and diverge below $y^+ = 10$.) But as is the case for Stress-ω, the $-\phi_{12}$ and $-D^T_{12}-\psi_{12}$ models used by LS act as reasonable models for $-\Pi_{12}$ and $-D^T_{12}$, which allows the difficulty associated with large near-wall pressure-transport $-\psi_{12}$ to be sidestepped.

Modeling deficiencies are also apparent in the $\phi_{22}-\varepsilon_{22}$ term in the LS $\overline{v'v'}$ budget (Fig. 11(b)). Although the model is able to reproduce the change from source to sink of $\phi_{22}-\varepsilon_{22}$ as the wall is approached, the LS and DNS magnitudes of the near-wall sink are very different. But despite this and other qualitative differences with the DNS, the budget errors compensate such that LS gives a better near-wall prediction of $\overline{v'v'}$ than the other two models do (see Figs. 8 and 9).

[3] Note however that the defining relationship between ϕ_{ij} and b_{ij} mentioned earlier does not hold below the logarithmic region.

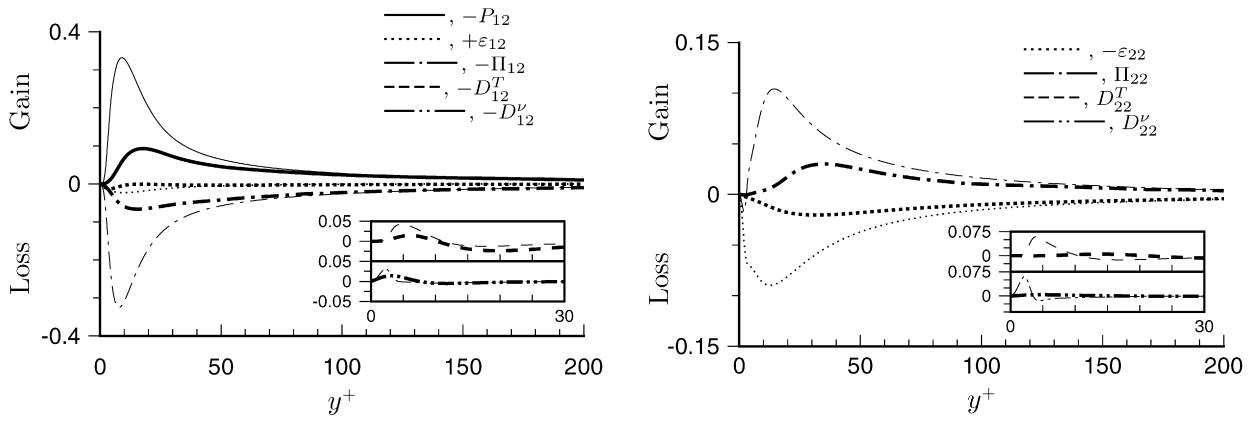

(a) SAYS $-\overline{u'v'}$ budget (b) SAYS $\overline{v'v'}$ budget

Fig. 12. Terms in the SAYS budget of (a) $-\overline{u'v'}$ and (b) $\overline{v'v'}$ Reynolds stresses for unstrained-channel flow at $Re_\tau = 390$. DNS results shown as thicker version of model curves. Normalization as in Fig. 10.

As with Stress-ω, the LS model also underestimates the influence of turbulent and pressure transport $D^T_{ij} + \psi_{ij}$. This is most apparent for the $-\overline{u'v'}$ and $\overline{v'v'}$ components (compare the thin- and thick-dashed lines in Fig. 11(a) and (b).) This is perhaps unsurprising, given that the LS $D^T_{ij} + \psi_{ij}$ model was admittedly constructed more for computational convenience than for accuracy, under the assumption that it is relatively unimportant in wall-bounded flows – although Launder and Shima did realize that DNS results were beginning to suggest that this was not strictly true [12]. But, as mentioned above, the practical significance of this formal modeling inconsistency is limited, due to compensating errors, primarily between the pressure–strain and turbulent transport models.

The SAYS budgets are similar to those for Stress-ω, in that excessive inner-layer $\overline{v'v'}$ leads to significant (although for SAYS not as extreme) over-predictions of $-P_{12}$ (Fig. 12(a)), and this too-large production is again mirrored by an exaggerated $-\Pi_{12}$. (Recall that unlike the other two closures, SAYS explicitly models the entire velocity–pressure-gradient correlation $\Pi_{ij} = \phi_{ij} + \psi_{ij}$ rather than just the pressure–strain term ϕ_{ij}.) The excess inner-layer $\overline{v'v'}$ observed in Fig. 8 is associated with the over-inflated ε_{22} and the improper near-wall behavior of the Π_{22} model (including spurious negative values) seen in Fig. 12(b) (see also b_{22} variation in Fig. 9(b)). The near-wall discrepancies in the SAYS Π_{22} model will be explored further in the next section.

Of the three models tested, SAYS is the only one to account explicitly for the near-wall anisotropy of ε_{ij}. And, as shown in Fig. 7(b), the SAYS ε profile is closest to the DNS. One might thus anticipate good SAYS predictions of all components of the near-wall dissipation ε_{ij}. Indeed SAYS is the only closure to locate the maximum dissipation of $\overline{u'u'}$ at the wall, where it belongs, although it is around 16% too large (not shown), presumably due to the large $\varepsilon_{\text{wall}}$ given by the SAYS dissipation equation (cf. Fig. 7(b)). The influence of ε_{12} encroaches into the buffer layer, rather than being confined to the very near-wall region. The SAYS ε_{22} is also much larger near the surface than the corresponding DNS term (with the peak around four to five times too large), and the maximum lies nearer to the wall than it should. These ε_{22} discrepancies are consistent with both the near-wall magnitude (too large) and location (too close to the surface) of the peak $\overline{v'v'}$ stress, since $\overline{v'v'}$ appears as a factor in the SAYS ε_{22} model.

The D^T_{ij} model used by SAYS is better than that used (for the $D^T_{ij} + \psi_{ij}$ sum) by Stress-ω and LS. Although its representation of D^T_{22} is not good, SAYS gives reasonable agreement with the DNS for $-D^T_{12}$ and especially the $\overline{u'u'}$ component D^T_{11} (not shown).

To summarize the unstrained-channel results, we note that the shortcomings in all three models are primarily associated with the near-wall behavior of their pressure–strain models. The manner in which these shortcomings are affected by application of the APG strain will be considered next.

4.2. 2D APG strained-channel predictions

The tests for this flow, which was generated by imposing an APG strain ($A_{11} = -A_{22} = -0.31 u_\tau(0)/h(0)$) on the $Re_\tau = 390$ channel turbulence, will center around the ability of the models to predict the time at which the wall

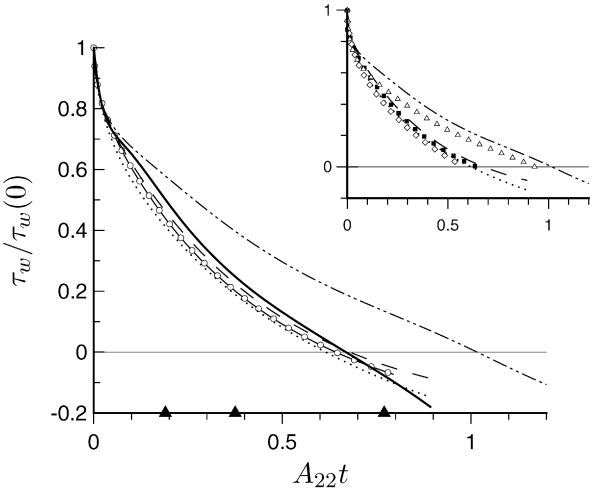

Fig. 13. DNS and model histories of wall shear stress τ_w for APG strain: —, DNS; - - -, Stress-ω; ···, LS; –···–, SAYS; ○, Menter SST two-equation model (results from [1]). Solid symbols along horizontal axis mark times for which wall-normal profiles are presented below. Subplot shows results using standard 'industrial' resolution ($\Delta y_1^+ = 0.5$, $y_{15}^+ = 30$): ■, Stress-ω; ◊, LS; Δ, SAYS. (Full-resolution results given by lines.)

shear stress τ_w becomes negative. Although this differs from the separation point of a spatial boundary layer in that here there is no mean streamline curvature and ejection of mean spanwise vorticity into the outer layer, the $\tau_w = 0$ prediction nevertheless reflects a model's ability to reproduce the cumulative effects of an APG. (The relevance of this test is supported by Yorke and Coleman's [1] finding that models known to predict either early or late separation in spatial APG layers also give respectively too small or too large $\tau_w = 0$ times for the APG strained-channel.) First- and second-order statistics will be examined, as will individual terms in the Reynolds-stress equations, by comparing them to the DNS results of [3].

The model and DNS skin-friction histories are shown in Fig. 13. The DNS curve is an interpolant through individual realizations [3] given by:

$$\tau_w(s)/\tau_w(0) = \exp(c_0 s) + c_1 s^3 + c_2 \exp(c_3 s)\sin(c_4 s),$$

where $s = A_{22}t$ and $(c_0, c_1, c_2, c_3, c_4) = (-3.5433, -0.3127, 2.9267, -29.5295, -3.3553)$. The estimated uncertainty in the DNS wall-stress reversal time, $A_{22}t = 0.675$, is ±5% [3].

The LS model underestimates this value by approximately 10% ($A_{22}t = 0.61$). On the other hand, the SAYS $\tau_w(t)$ does not change sign until $A_{22}t = 1.02$. The Stress-ω prediction of the wall-stress reversal time is $A_{22}t = 0.68$, which is just 0.75% larger than the DNS value. This performance is better than that given by all the lower-order models tested in [1], although one of them (Menter's two-equation SST, denoted in Fig. 13 by the open symbols) is just within the ±5% uncertainty of the DNS, with its slightly too-early prediction of 0.64.

The subplot shown in Fig. 13 reveals the effect of using 'industrial' resolution for each of the three models. This involved replacing the 400 points between the wall and the channel centerline with 28, such that the first grid point off the wall is at $y_0^+ = 0.5$ and only 15 points lie between $y^+ = 0$ and $y_0^+ = 30$. (No change was made to the timestep, with $\Delta t u_\tau^2(0)/\nu$ again equal 1.25×10^{-2} for Stress-ω and LS, and 1.25×10^{-3} for SAYS.) These values were chosen because they are typical of RANS calculations of complex-geometry flows of industrial interest. While the wall-stress histories of all three closures are affected, and each reach $\tau_w = 0$ sooner than the full-resolution runs do, the influence of the change is most profound for SAYS (the symbols indicate the industrial-resolution results, the lines the full-resolution histories). This, along with its smaller Δt requirement, implies that the SAYS formulation is characterized by more numerical stiffness than are the other two schemes.

The model and DNS mean velocities at $A_{22}t = 0.365$ and 0.77 are shown in Figs. 14 and 15. Although the Stress-ω results are marginally best at $A_{22}t = 0.365$, in contrast to the unstrained case none of the closures is especially good at matching the DNS over the entire layer – an indication of the modeling challenge introduced by the APG strain. The inner-scaling velocities do however follow qualitative trends exhibited by the DNS, in particular the departure from the logarithmic law of the wall. (The difference between the $A_{22}t = 0.365$ profile and the $A_{22}t = 0$ initial condition

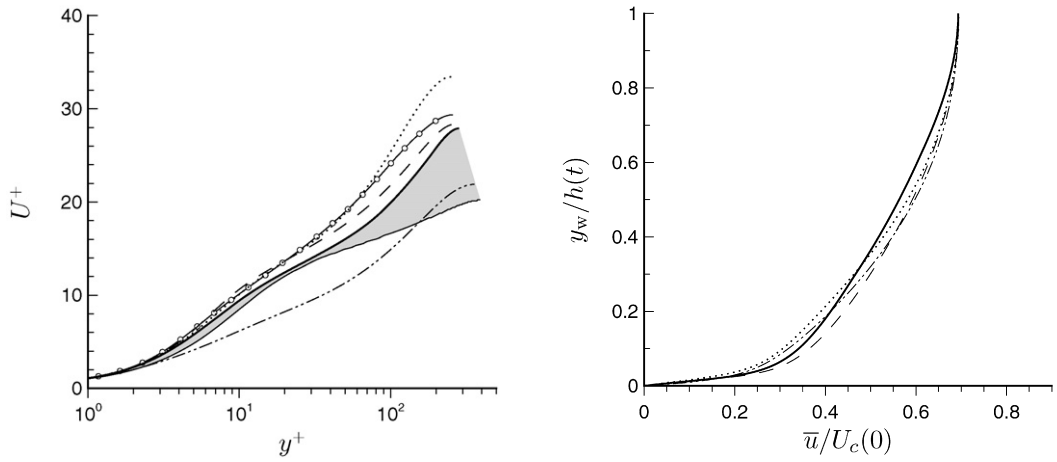

Fig. 14. DNS and model predictions of mean velocity in (a) inner- and (b) outer-layer scaling for APG strain at $A_{22}t = 0.365$: —, DNS; - - -, Stress-ω; ⋯, LS; –·–, SAYS; ○, Menter SST (in (a) only; from [1]). Velocities measured with respect to coordinate system attached to streamwise moving walls (cf. Fig. 2). Shaded region in (a) indicates change of DNS from unstrained initial condition, denoted by thin-solid (—) curve.

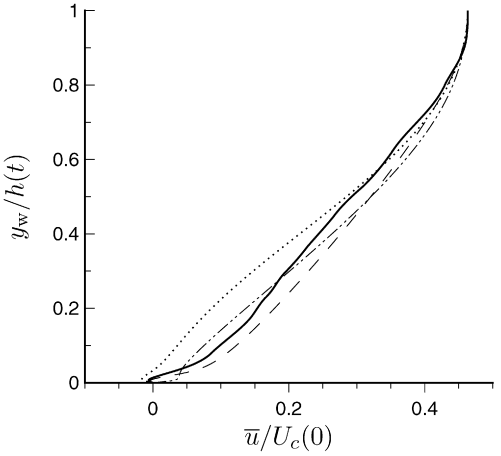

Fig. 15. DNS and model predictions of mean velocity in outer-layer scaling for APG strain at $A_{22}t = 0.77$: —, DNS; - - -, Stress-ω; ⋯, LS; –·–, SAYS. Velocities measured with respect to coordinate system attached to streamwise moving walls (cf. Fig. 2).

observed in the DNS is indicated by the shaded region in Fig. 14(a); also shown, via the open symbols, is the SST result, which of the four lower-order models tested in [1] gave the best agreement for this quantity.) The excessive u_τ given by SAYS (cf. Fig. 13) is at least partially responsible for the striking under-prediction of the mean velocity in the inner-layer scaling.

The $-\overline{u'v'}$ shear-stress profiles for $A_{22}t = 0.19$ and 0.365 in Fig. 16 reveal that the model-DNS mismatch increases with time. The Stress-ω model comes closest to the trends observed in the DNS, although the agreement is not exact. The greatest error is given by SAYS, which exaggerates the $-\overline{u'v'}$ growth in proportion to the over-prediction of u_τ (Fig. 13). Normal-stress statistics are shown in Figs. 17 and 18. While the agreement with the DNS is not especially good, the LS model does manage to capture qualitative features of the $\overline{u'u'}$ and $\overline{v'v'}$ profiles as they develop in time. For example, at $A_{22}t = 0.365$, this model best reproduces the magnitude and location of the near-wall peak $\overline{u'u'}$ (Fig. 17(b)), a feature completely missed by the other two schemes. The tendency, observed above for the unstrained flow, for the Stress-ω model to grossly under-predict $\overline{u'u'}$ and over-predict $\overline{v'v'}$ is again apparent.

Figs. 19 and 20 present the Stress-ω budgets for the APG flow for $-\overline{u'v'}$ and $\overline{v'v'}$ at $A_{22}t = 0.19$. The former shows that the isotropic ε_{ij} assumption used by Stress-ω and LS is not seriously compromised by the application of

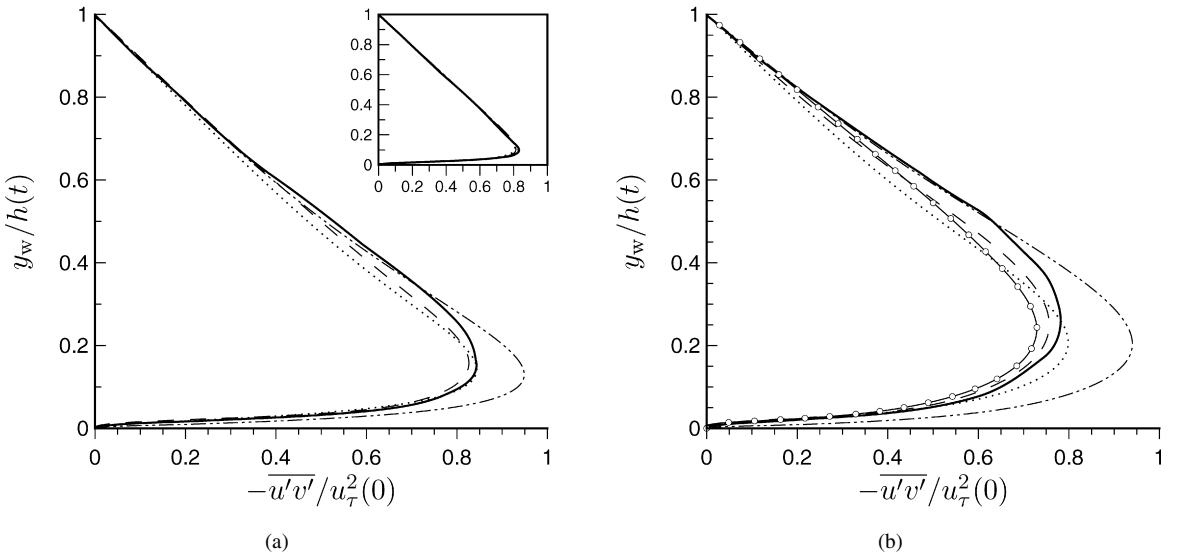

Fig. 16. DNS and model predictions of Reynolds shear stress $-\overline{u'v'}$ for APG strain at (a) $A_{22}t = 0.19$ and (b) $A_{22}t = 0.365$: —, DNS; - - -, Stress-ω; · · ·, LS; –·–, SAYS; ∘, Menter SST two-equation model results from [1] (in (b) only). Subplot in (a) illustrates state at $A_{22}t = 0$.

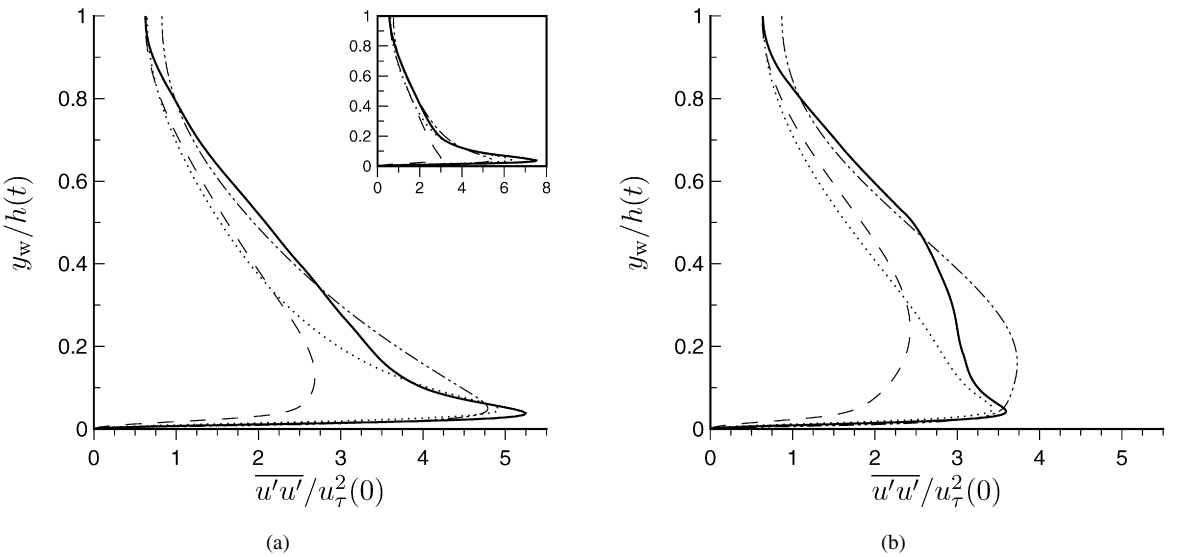

Fig. 17. DNS and model predictions of Reynolds normal stress $\overline{u'u'}$ for APG strain at (a) $A_{22}t = 0.19$ and (b) $A_{22}t = 0.365$: —, DNS; - - -, Stress-ω; · · ·, LS; –·–, SAYS. Subplot in (a) illustrates state at $A_{22}t = 0$ (from Fig. 8(a)).

the $A_{11} = -A_{22} < 0$ strain. On the other hand, the $-\overline{u'v'}$ production is important. Even with the straining, it again reduces to $-P_{12} = \overline{v'v'}\,\partial\overline{u}/\partial y$, since the applied-straining component $P_{12}^A = \overline{u'v'}(A_{11} + A_{22})$ is zero for the APG strain. Stress-ω again dramatically over-predicts $-P_{12}$, due in large part to its profound overestimation of $\overline{v'v'}$. This in turn also leads to an exaggerated $-\phi_{12}$, since terms involving the production tensor dominate the Stress-ω model for ϕ_{ij} (the other terms in the model tend to cancel each other, as they do for the unstrained-channel flow). The ϕ_{ij} model, through the dependence of the rapid component ϕ_{ij}^R upon P_{ij}, is at least able to qualitatively emulate the classic 'extra-strain' effect observed in the DNS, that the applied strain causes changes of opposite sign in two large terms (here $-P_{12}^S$ and $-\phi_{12}$), the imbalance of which controls the overall $\overline{u_i'u_j'}$ evolution. The success of the Stress-ω pressure–strain model (and indeed of those used by LS and SAYS) is defined by how well the rapid, slow and near-wall combination is able to quantify this strain-induced 'tug-of-war' process. For Stress-ω, large errors in individual

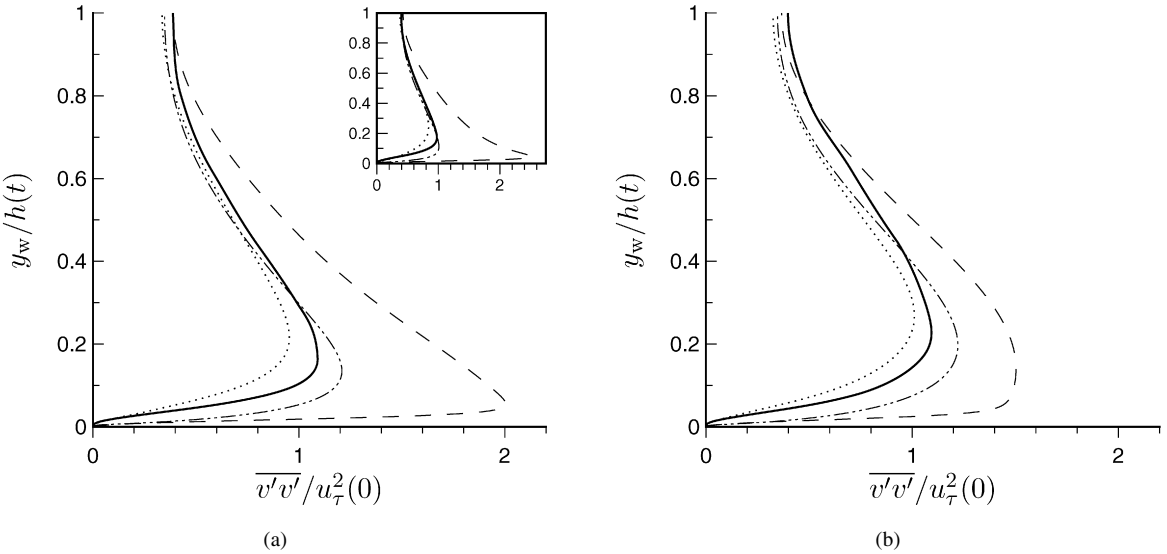

Fig. 18. DNS and model predictions of Reynolds normal stress $\overline{v'v'}$ for APG strain at (a) $A_{22}t = 0.19$ and (b) $A_{22}t = 0.365$: —, DNS; - - -, Stress-ω; ···, LS; –·–, SAYS. Subplot in (a) illustrates state at $A_{22}t = 0$ (from Fig. 8(b)).

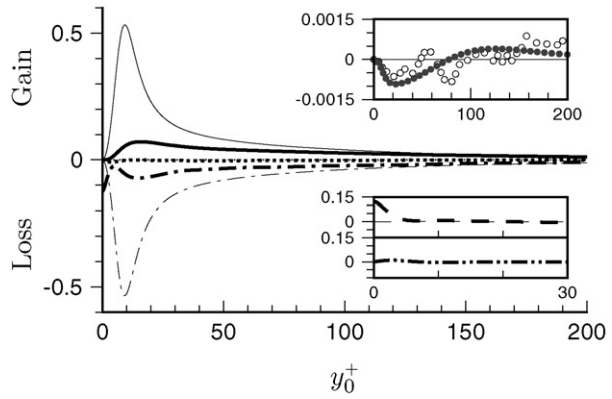

Fig. 19. Terms in the Stress-ω budget of the Reynolds shear stress $-\overline{u'v'}$ for APG strain at $A_{22}t = 0.19$: —, $-P_{12}^S$; ···, $+\varepsilon_{12}$; –·–, $-\phi_{12}$; - - -, $-D_{12}^T - \psi_{12}$; –···–, $-D_{12}^\nu$. DNS results shown as thicker version of model curves. Symbols denote sum of all terms ($\approx -\partial\overline{u'v'}/\partial t$): ∘, DNS; •, Stress-$\omega$. Budget terms normalized by $u_\tau^4(0)/\nu$; wall-normal coordinate $y_0^+ = y_w \exp(-A_{22}t)u_\tau(0)/\nu$.

terms tend to cancel each other, so that the overall $-\partial\overline{u'v'}/\partial t$ prediction is not too dissimilar to that given by the DNS. Note also that the $-\phi_{12}$ and $-(D_{12}^T + \psi_{12})$ model combination used by Stress-ω again (as for the unstrained case) produces approximately the same net effect near the wall as these two terms do in the DNS – despite the fact that each of the Stress-ω pair go to zero at the wall, while in the DNS $-\phi_{12}$ and $-(D_{12}^T + \psi_{12})$ approach large values of opposite sign as $y_w \to 0$.

Although the production term $P_{22} = P_{22}^A = -2\overline{v'v'}A_{22}$ in the $\overline{v'v'}$ budget (Fig. 20) is no longer zero, as a result of the applied APG strain[4], it is much smaller than both the pressure–strain and dissipation terms, whose imbalance $\phi_{22} - \varepsilon_{22}$ dominates the sign and magnitude of the net rate of change of $\overline{v'v'}$ over most of the flow. Near the wall, however, P_{22}^A has a controlling influence on the Stress-ω prediction, not only because it is too large (since $\overline{v'v'}$ is) but also because it is responsible, along with the too-large ε_{22} and too-small $D_{22}^T + \psi_{22}$ (and is only partially counteracted by the non-zero viscous transport D_{22}^ν near the wall), for the exaggerated negative $\partial\overline{v'v'}/\partial t$ over the lower quarter

[4] The $\overline{v'v'}$ 'production' P_{22} is negative here.

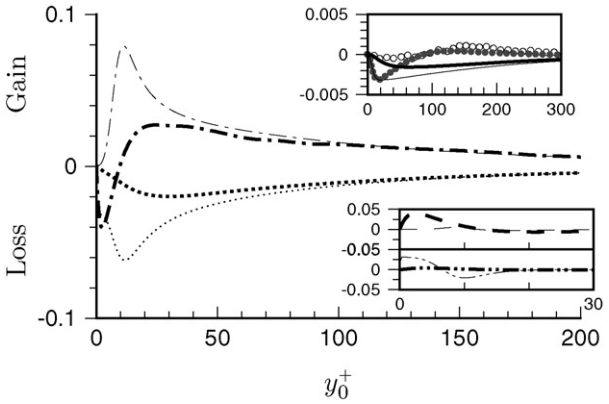

Fig. 20. Terms in the Stress-ω budget of the wall-normal Reynolds normal stress $\overline{v'v'}$ for APG strain at $A_{22}t = 0.19$: —, P_{22}^A; $\cdots$, $-\varepsilon_{22}$. –·–, ϕ_{22}; - - -, $D_{22}^T + \psi_{22}$; –··–, D_{22}^ν. DNS results shown as thicker version of model curves. Symbols denote sum of all terms ($\approx \partial\overline{v'v'}/\partial t$) at $A_{22}t = 0.19$: ○, DNS; •, Stress-ω. Normalization as in Fig. 19.

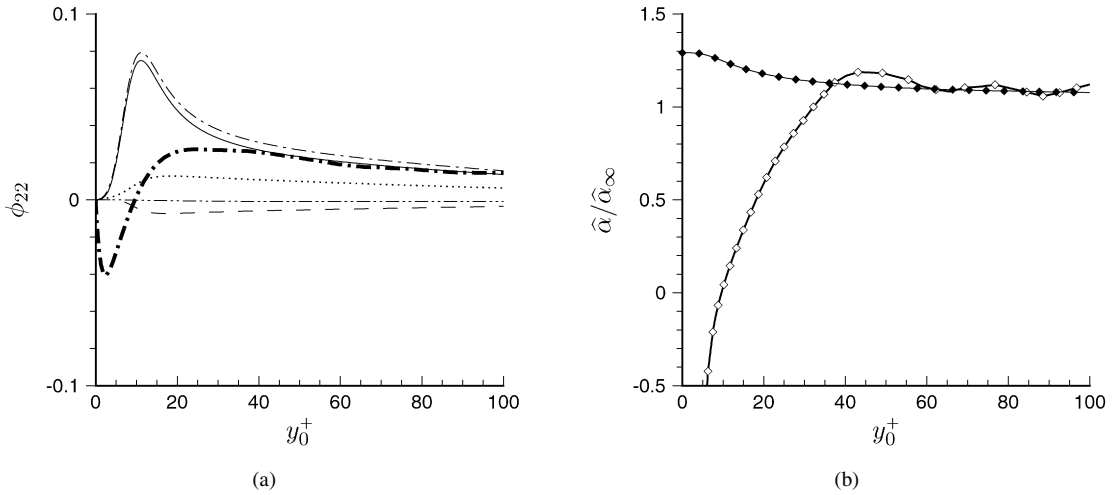

Fig. 21. (a) Components of Stress-ω ϕ_{22} model in Fig. 20: –·–, ϕ_{22} (thinner and thicker curves respectively indicate Stress-ω and DNS results); $\cdots$, $-C_1\beta^*\omega(\overline{v'v'} - \frac{2}{3}k)$; —, $-\hat{\alpha}(P_{22}^A - \frac{2}{3}\mathcal{P})$; - - -, $-\hat{\beta}(D_{22} - \frac{2}{3}\mathcal{P})$ –·–, $-\hat{\gamma}kA_{22}$. (b) Dominant low-Reynolds-number correction to the Stress-ω ϕ_{22} model: ♦, $\hat{\alpha}/\hat{\alpha}_\infty$ (Stress-ω); ◊, $-\phi_{22}/[\hat{\alpha}_\infty(P_{22}^A - \frac{2}{3}\mathcal{P})]$ (DNS). Production $\mathcal{P} = \frac{1}{2}(P_{ii}^S + P_{ii}^A)$. Normalization as in Fig. 19.

of the channel (compare solid and open symbols in Fig. 20 subplot). The practical effect of this error, however, is beneficial, since it leads to rapid near-wall reduction of the Stress-ω $\overline{v'v'}$ profile. But because this reduction occurs to a quantity that is initially much too large (Fig. 18(a) subplot), the agreement between the Stress-ω results at $A_{22}t = 0.19$ and 0.365, and the DNS is not good (although the difference is less at the later time). The model performance for the unstrained plane channel therefore has a significant impact on its ability to capture the effects of the strain – which points to the value of using simple canonical flows to design and calibrate closures.

The near-wall corrections to the Stress-ω pressure–strain model again fail to reproduce the change of sign found in the DNS. As is the case for the unstrained flow, this errant behavior is largely due to the low-Reynolds-number correction to the $\hat{\alpha}$ term. This can be inferred from Fig. 21(a), which illustrates the components of the Stress-ω ϕ_{22} model. It is dominated by the first of the rapid-pressure terms $\phi_{22}^{R\,(1)} = -\hat{\alpha}(P_{22}^A - \frac{2}{3}\mathcal{P})$ (see (3.17) and compare chain-dot and solid lines). The fact that $\phi_{22} \approx \phi_{22}^{R\,(1)}$ allows us to use the DNS results to obtain an estimate of the near-wall modification of ϕ_{22} required for the Stress-ω to reproduce the near-wall $\overline{v'v'}$ variation. This is presented in Fig. 21(b), where the actual Stress-ω correction $\hat{\alpha}/\hat{\alpha}_\infty$ can be compared to the ratio $-\phi_{22}/[\hat{\alpha}_\infty(P_{22}^A) - \frac{2}{3}\mathcal{P}]$ from the DNS. While in the outer layer the agreement is good, near the wall they are very different, both in magnitude and sign.

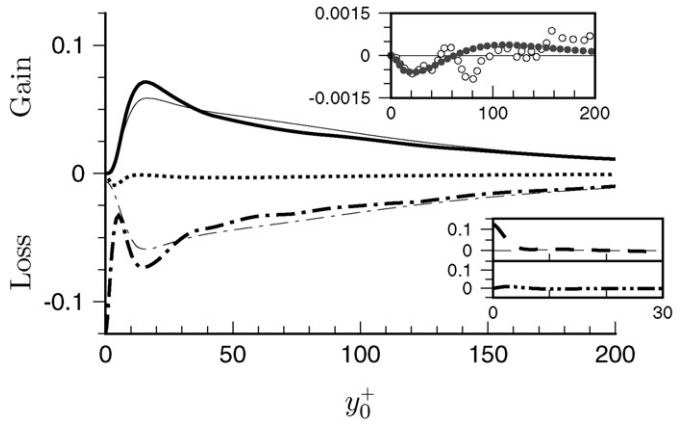

Fig. 22. Terms in the LS budget of the Reynolds shear stress $-\overline{u'v'}$ for APG strain at $A_{22}t = 0.19$: —, $-P_{12}^S$; ···, $+\varepsilon_{12}$ (DNS only); –·–, $-(\phi_{12} - \varepsilon_{12})$ - - -, $-D_{12}^T - \psi_{12}$; –···–, $-D_{12}^\nu$. DNS results shown as thicker version of model curves. Symbols denote sum of all terms ($\approx -\partial\overline{u'v'}/\partial t$) at $A_{22}t = 0.19$: ∘, DNS; •, LS. Normalization as in Fig. 19.

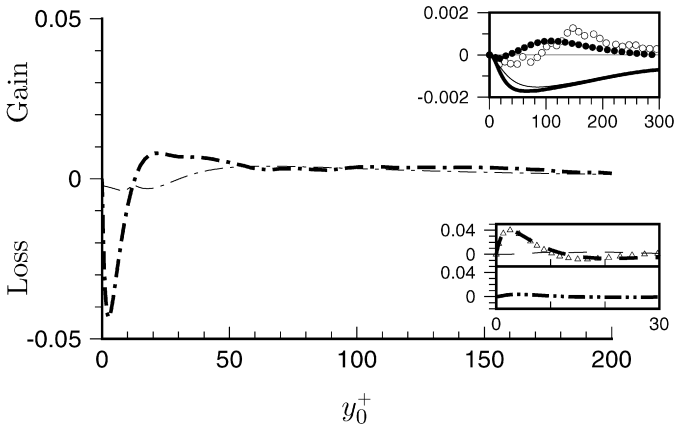

Fig. 23. Terms in the LS budget of the wall-normal Reynolds normal stress $\overline{v'v'}$ for APG strain at $A_{22}t = 0.19$: —, P_{22}^A; –·–, $\phi_{22} - \varepsilon_{22}$; - - -, $D_{22}^T + \psi_{22}$; Δ, ψ_{22} (DNS only); –···–, D_{22}^ν. DNS results shown as thicker version of model curves. Symbols in upper subplot denote sum of all terms ($\approx \partial\overline{v'v'}/\partial t$) at $A_{22}t = 0.19$: ∘, DNS; •, LS. Normalization as in Fig. 19.

The LS budgets are shown in Figs. 22 and 23. The contributions of the pressure–strain and dissipation terms are again combined, given the ϕ_{ij} model's near-wall modifications to account for the anisotropy of ε_{ij}. The somewhat too large $-\overline{u'v'}$ production $-P_{12} = \overline{v'v'}\,\partial\bar{u}/\partial y$ in the region $50 < y_0^+ < 200$ (Fig. 22) is related to the inflated mean velocity gradient given here by LS (cf. Fig. 14(a)). At the same time, the underprediction of $\overline{v'v'}$ by LS leads to the diminished maximum $-P_{12}$ production observed in Fig. 22 (the near-wall LS velocity gradients are comparable to the DNS results). We find that the errors in the $-\overline{u'v'}$ production are mirrored in the $-\phi_{12} + \varepsilon_{12}$ term, through the dependence of the rapid-pressure–strain model $-\phi_{12}^R$ on $-P_{12}$ (see Eq. (3.9)), but the net effect is a $-\partial\overline{u'v'}/\partial t$ prediction not far from that found in the DNS at this time (symbols in Fig. 22 subplot). As with the unstrained flow (cf. Fig. 10(a)), the influence of LS's use of $-\phi_{12}$ rather than $-\Pi_{12}$ (and of including the pressure transport in the turbulent transport model) is mitigated by the errors in the individual $-\phi_{12}$ and $-(D_{12}^T + \psi_{12})$ models tending to compensate such that near the wall their sum is close to that found in the DNS.

The $\overline{v'v'}$ budget in Fig. 23 reveals a large discrepancy between the pressure–strain/dissipation sum $\phi_{22} - \varepsilon_{22}$ given by LS and that found in the DNS (thin and thick chain-dot lines). Also shown, in Fig. 24(a), for reference, are the DNS and model profiles of the individual ϕ_{22} (chain-dot) and ε_{22} (dotted) terms. The corresponding kinetic energy dissipation ε is given in Fig. 25(b). These should be interpreted with care, especially near the wall, given that LS makes no attempt to capture the effect of the wall on ε_{ij}, with all near-wall corrections applied to ϕ_{ij}. We note the

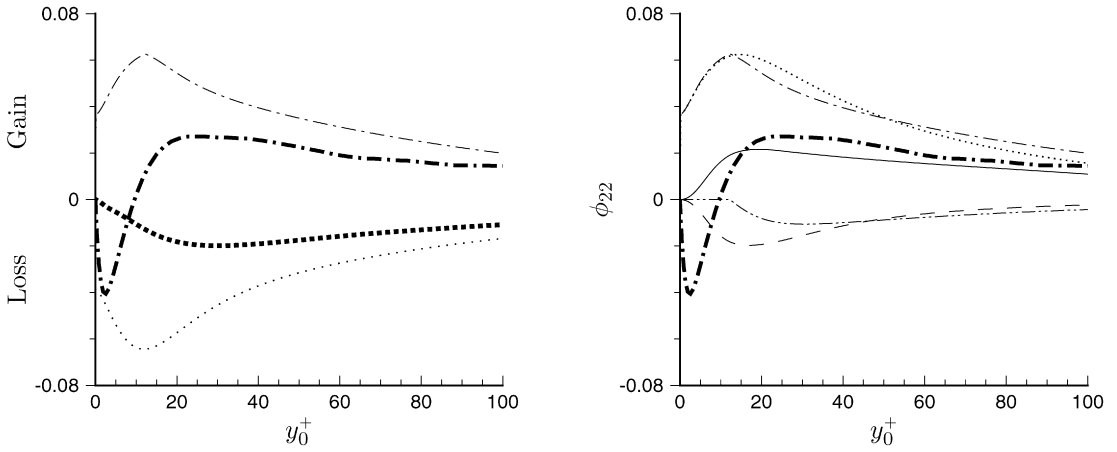

Fig. 24. (a) Selected terms in the LS budget of the wall-normal Reynolds normal stress $\overline{v'v'}$ for APG strain at $A_{22}t = 0.19$: –·–, ϕ_{22}; ···, $-\varepsilon_{22}$. (b) Components of LS ϕ_{22} model (see Eq. (3.7)): –·–, ϕ_{22}; ···, ϕ_{22}^S; —, ϕ_{22}^R; - - -, $\phi_{22\,W}^S$; –··–, $\phi_{22\,W}^R$. DNS results shown as thicker version of model curves for ϕ_{22} and $-\varepsilon_{22}$ in (a) and ϕ_{22} in (b)). Normalization as in Fig. 19.

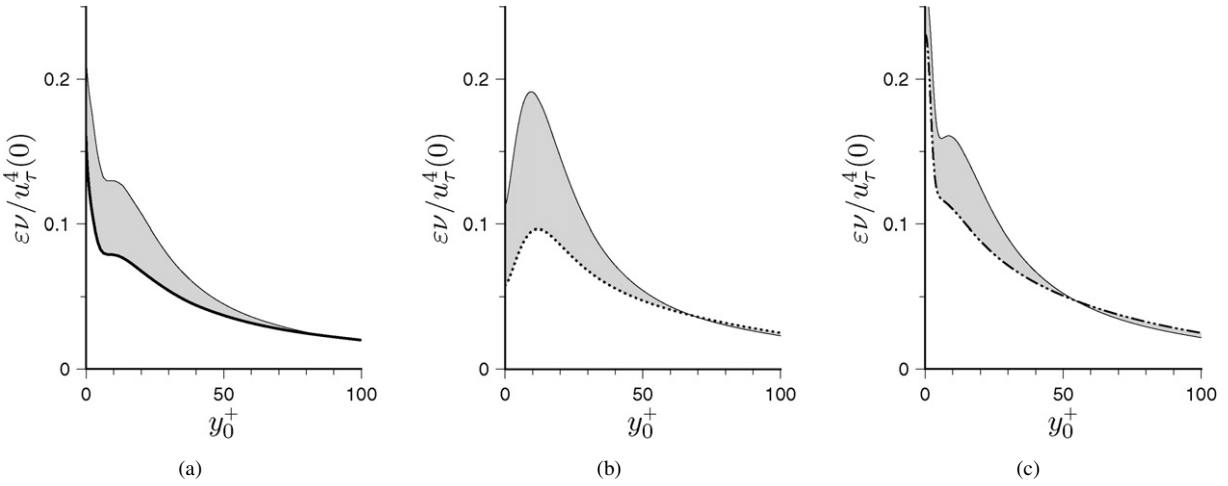

Fig. 25. Rate of turbulence kinetic energy dissipation ε given by (a) DNS, (b) LS and (c) SAYS for APG strain at $A_{22}t = 0.19$: Shaded regions indicate change from unstrained initial condition (as in Fig. 7(b)), denoted by thin-solid curve.

tendency for the LS models to exaggerate the magnitudes of both the pressure–strain and dissipation over the inner and outer regions, compared to the DNS. (Here the ϕ_{22} model is dominated by the return-to-isotropy term ϕ_{22}^S; see (3.8)–(3.10) and Fig. 24(b).) In the outer region, this leads to no serious difficulty, as the $\phi_{22} - \varepsilon_{22}$ imbalance agrees well with the DNS. However, LS gives a poor representation of the large near-wall minimum $\phi_{22} - \varepsilon_{22}$ in the DNS (associated with ϕ_{22}). This is to some extent overcome by the fortuitous failure of the $D_{22}^T + \psi_{22}$ gradient-diffusion model, which effectively neglects the ψ_{22} component (compare thin- and thick-dash curves in Fig. 23 subplot; the open triangles indicates ψ_{22} from the DNS). But despite these large discrepancies, especially in the near-wall ϕ_{22}, the LS terms combine to give a net $\partial\overline{v'v'}/\partial t$ prediction that is, if not ideal, much better than one might expect after examining the behavior of the ϕ_{22} model. The LS performance for the $\overline{u'u'}$ budget (not shown) is even better. Although the maximum dissipation is once more (as for the $A_{ij} = 0$ case) erroneously located off the wall, the LS $\phi_{11} - \varepsilon_{11}$ is quite successful in emulating the net $\partial\overline{u'u'}/\partial t$ from the DNS (see [28]). Of the three closures, LS is best at duplicating the evolution of the magnitude and location of the peak $\overline{u'u'}$, and its overall $\overline{u'u'}$ profile is distinctly better than that given by Stress-ω (Fig. 17).

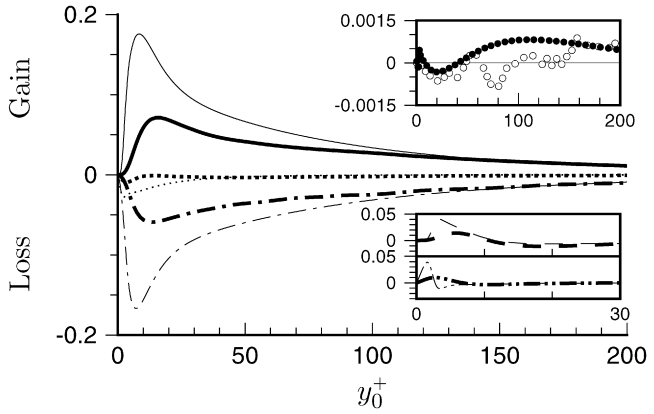

Fig. 26. Terms in the SAYS budget of the Reynolds shear stress $-\overline{u'v'}$ for APG strain at $A_{22}t = 0.19$: —, $-P_{12}^S$; –·–·–, $-D_{12}^\nu$; - - -, $-D_{12}^T$; –··–, $-\Pi_{12}$; ···, $+\varepsilon_{12}$. DNS results shown as thicker version of model curves. Symbols denote sum of all terms ($\approx -\partial\overline{u'v'}/\partial t$) at $A_{22}t = 0.19$: ∘, DNS; •, SAYS. Normalization as in Fig. 19.

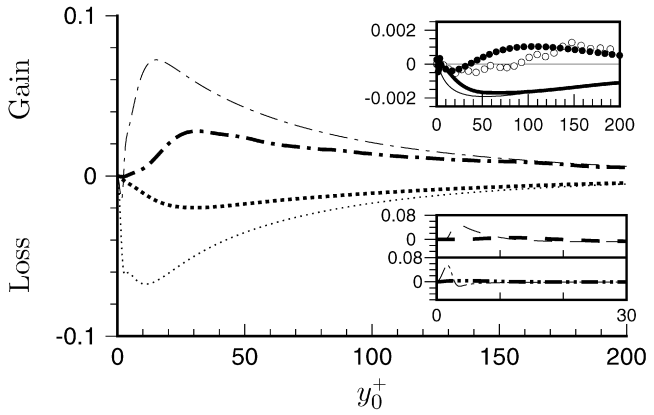

Fig. 27. Terms in the SAYS budget of the wall-normal Reynolds normal stress $\overline{v'v'}$ for APG strain at $A_{22}t = 0.19$: —, P_{22}^A; –·–·–, D_{22}^ν; - - -, D_{22}^T; –··–, Π_{22}; ···, $-\varepsilon_{22}$. DNS results shown as thicker version of model curves. Symbols denote sum of all terms ($\approx \partial\overline{v'v'}/\partial t$) at $A_{22}t = 0.19$: ∘, DNS; •, SAYS. Normalization as in Fig. 19.

From the SAYS $-\overline{u'v'}$ budgets in Fig. 26, we again find the balance is dominated by the $-P_{12}$ and $-\Pi_{12}$ terms, both of which (as for the unstrained channel) have amplitudes much larger than they should. (Recall that unlike Stress-ω and LS, SAYS explicitly accounts for both the pressure–strain ϕ_{ij} and pressure transport ψ_{ij} in its Π_{ij} model, rather than implicitly folding ψ_{ij} into a gradient-diffusion transport model for D_{ij}^T.) The $-P_{12}$ overprediction is a symptom of the somewhat inflated near-wall $\overline{v'v'}$, observed in Fig. 18. The velocity–pressure-gradient model $-\Pi_{12}$ faithfully balances the errant production, primarily through the rapid components $\alpha_1 P_{12} + \beta_1 D_{12} + (2\gamma_1 + C_3^* \Pi^{1/2}) k S_{12}$, which are dominant. (The β_1 and S_{12} terms are largest, and being of opposite sign, roughly cancel each other.) The model $-\overline{u'v'}$ dissipation ε_{12} in Fig. 26 has a larger peak value, which is closer to the wall, than the DNS benchmark. This is a consequence at least in part of the excessive near-wall $-\overline{u'v'}$ given by this closure (since $-\overline{u'v'}$ appears as a factor in the SAYS ε_{12}). The ε_{12} disparity is also a result of inaccuracy in the rate of kinetic energy dissipation ε (Fig. 25(c)), which also contributes to the exaggerated ε_{22} near the wall (Fig. 27). The excessive near-wall $\overline{v'v'}$ is another factor in the inflated ε_{22}, and it is also associated with the spurious near-wall values of the molecular and turbulent transport D_{22}^ν and D_{22}^T, illustrated in Fig. 27 (lower subplots).

Large qualitative differences between SAYS and the DNS are also found in the velocity–pressure-gradient term Π_{22}, which erroneously acts as a sink very near the wall. To better understand this behavior, we consider in Fig. 28 the separate components of the SAYS Π_{22} model (cf. Eq. (3.13)). This reveals that the near-wall negative value of Π_{22} is a result of the pressure transport model ψ_{22}, caused by the exaggerated molecular transport D_{22}^ν in

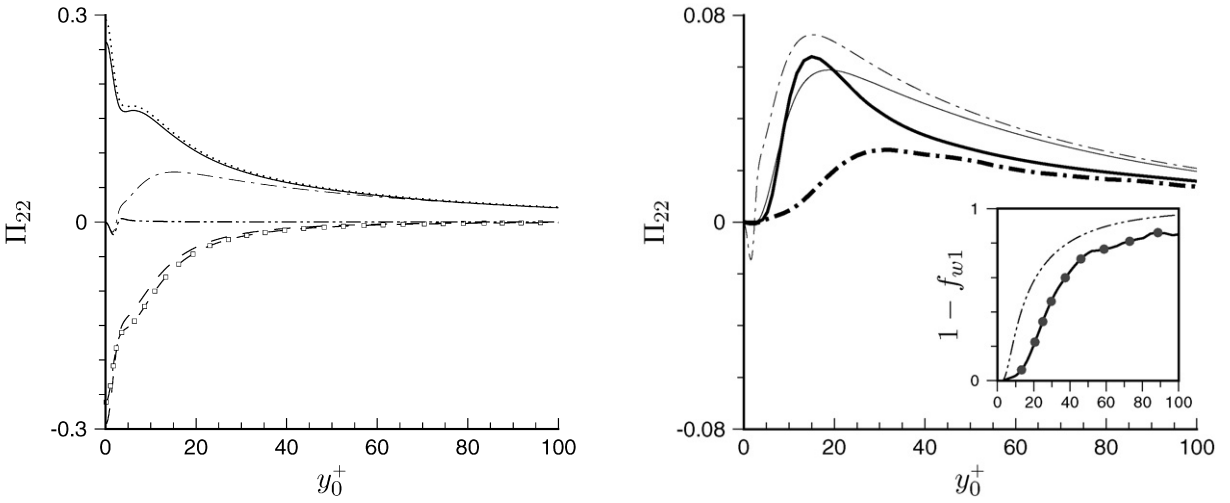

Fig. 28. Decomposition of SAYS Π_{22} model for APG strain at $A_{22}t = 0.19$. Part (a): –·–, Π_{22}; ···, $\Pi_{22} - \phi_{22}^W - \psi_{22}$; —, $\phi_{22}^* = -(C_1\varepsilon + C_1^*\mathcal{P})b_{22}$; - - -, ϕ_{22}^W; □, $-f_{w1}\phi_{22}^*$ –···–, ψ_{22}. Part (b): –·–, Π_{22}; —, $(1-f_{w1})\phi_{22}^*$; –···–, $1-f_{w1}$ (SAYS); •, Π_{22}/ϕ_{22}^* (DNS). DNS results (or SAYS model using DNS values) shown as thicker version of model curves. Production $\mathcal{P} = \frac{1}{2}(P_{ii}^S + P_{ii}^A)$. Normalization as in Fig. 19.

the vicinity of the wall (Eq. (3.14b) becomes $\psi_{22} = -\frac{1}{3}D_{22}^{\nu}$). Fig. 28(a) also implies that the first two terms (the slow/return-to-isotropy and the first rapid term, $\sim \mathcal{P}b_{22}$) are the dominate ones. (The sum of the other (α_1, β_1 and S_{22}) rapid terms, which are somewhat smaller, is essentially zero.) This can be seen by the agreement between the dotted and solid curves (the former indicating the sum of all but the wall-damping ϕ_{22}^W and pressure-transport ψ_{22} terms in the Π_{22} model, the latter $-(C_1\varepsilon + C_1^*\mathcal{P})b_{22}$). Further evidence is given by the fact that the entire damping term can be represented to a good approximation by $f_{w1}(C_1\varepsilon + C_1^*\mathcal{P})b_{22})$, where f_{w1} is the near-wall damping function (compare dashed line and open symbols in Fig. 28(a)). As a result, it is reasonable to reduce the $\overline{v'v'}$ component of the SAYS model to $(1-f_{w1})\phi_{22}^*$, where $\phi_{22}^* = -(C_1\varepsilon + C_1^*\mathcal{P})$. The difference between the full and truncated models can be seen in Fig. 28(b), by comparing the chain-dot and solid lines. Also shown in Fig. 28(b) (denoted by the thicker curves) are the corresponding actual Π_{22} from the DNS and the truncated model ϕ_{22}^* constructed from the DNS data. Both the model and DNS results indicate the excessive near-wall Π_{22} is primarily due to the inability of the SAYS function f_{w1} to provide sufficient damping. This message is reinforced by the Fig. 28(b) subplot, which illustrates both the near-wall damping used by SAYS, $f_{w1} = \exp(-(Re_t/200)^2)$, where $Re_t = k^2/\nu\varepsilon$ (thin broken line), as well as the effective damping inferred by the DNS, using the $\Pi_{22} \approx (1-f_{w1})\phi_{22}^*$ approximation (solid symbols). For the $\overline{v'v'}$ component of this flow, better results would be obtained if the damping function were to fall off with wall-normal distance at a rate slower than the SAYS formulation prescribes.

4.3. Recap of results and implications

The first part of the study involved checking predictions for unstrained plane-channel flow at $Re_\tau = 390$. The Stress-ω model is best at reproducing the mean velocity, and in particular yields a skin-friction coefficient and law-of-the-wall profile that best agree with the DNS. All three closures exhibit deficiencies in the near-wall behavior of their pressure–strain ϕ_{ij} models. For Stress-ω this results in a poor representation of the near-wall normal-stress anisotropy, and in wall-normal stresses $\overline{v'v'}$ that are much too large. This in turn has a large adverse effect on the other Reynolds stresses, and exaggerates their production and pressure–strain terms. Nevertheless, compensating errors in the Stress-ω terms in the $-\overline{u'v'}$ equation yield the best agreement with the plane-channel DNS. Both LS and SAYS slightly under-estimate the peak value of the shear stress. However, both give reasonably good predictions of the normal stresses. The near-wall distribution of $\overline{v'v'}$ by LS, and the very-near-wall distribution of $\overline{u'u'}$ by SAYS, in particular are very close to that of the DNS, pointing to the success of the near-wall terms for these components of their pressure–strain models. (The same cannot be said of the other components.) Although they yield less accurate

mean-velocity predictions, both LS and SAYS give high-quality approximations to the normal-stress anisotropy near the wall. In contrast, the streamwise and wall-normal stresses from Stress-ω remain nearly equal as $y_w \to 0$.

Besides limitations in the pressure–strain models near the wall, a common characteristic exhibited by all three closures when applied to the plane channel is the beneficial tendency for errors in individual terms to cancel each other. This is most obvious for the schemes (Stress-ω and LS) that neglect the pressure-transport term ψ_{ij} (by including it in the gradient-diffusion model for the turbulent transport D_{ij}^T), and work with the pressure–strain term ϕ_{ij} rather than the velocity–pressure-gradient correlation $\Pi_{ij} = \phi_{ij} + \psi_{ij}$. Although ψ_{ij} is not small, and thus the difference between Π_{ij} and ϕ_{ij} not insignificant, since ψ_{ij} and ϕ_{ij} are of comparable magnitude and of opposite sign near the wall, and since the Stress-ω and LS pressure–strain and transport both approach zero near the wall, the practical consequence for Stress-ω and LS of neglecting ψ_{ij} is not especially serious for the unstrained flow. Their $-\overline{u'v'}$ predictions, for example, are of no less quality for the plane channel than that by SAYS, which explicitly accounts for D_{ij}^T and ψ_{ij}.

It is perhaps no surprise that the modeling deficiencies observed in the unstrained plane channel are amplified in the strained flow – if for no other reason than that each model's prestrained plane-channel prediction is used as initial conditions for the strained-channel test. (If this had not been done, it would not have been possible to differentiate between transients associated with relaxing towards the model's steady state and changes induced by the APG strain.) This amplification of model shortcomings causes the error-compensation process active for the plane channel to, although not disappear, become less efficient once the APG strain is applied.

For the non-zero $A_{11} = -A_{22} < 0$ flow, Stress-ω best reproduces the cumulative effect of the APG deformation, when measured in terms of the near-wall mean velocity profile and the time (to within less than 1%) at which the surface shear stress becomes negative. By way of contrast, in a test of lower-order models for the same flow [1], the best prediction was given by the Menter SST model, which came within 5% of the $\tau_w = 0$ time from the DNS. The LS closure underestimates the near-wall $\bar{u}$ and thus under-predicts the stress-reversal time by about 10%. SAYS delays this temporal version of separation, giving a consistently too-large value of wall-shear stress throughout the straining period. (Interestingly, when compared to DNS of another strained-channel idealization, this one emulating a swept-wing boundary layer [2], by applying both APG and sideways-skewing deformations, the opposite occurs – the SAYS prediction of the time at which $(\tau_w)_x$ changes sign is too early [26].) In addition to giving the best agreement with $-\overline{u'v'}$ from the unstrained initial-condition DNS, Stress-ω also best represents the evolution of this statistic during the straining period. But Stress-ω also yields normal-stress predictions that are much poorer (as it did when $A_{11} = A_{22} = 0$) than those from LS and SAYS, largely because of deficiencies in the near-wall pressure–strain model. The errant normal-stress predictions of Stress-ω (and in particular the fact that the streamwise $\overline{u'u'}$ and wall-normal $\overline{v'v'}$ components are essentially equivalent, even for the unstrained channel) does not bode well for when it is applied to more general cases. For the parallel strained-channel geometry, the effect of the normal-stress mismatch is relatively benign. But for spatial flows with separation (which include mean streamline curvature and therefore non-zero $\partial\bar{v}/\partial x$) the ability to correctly capture the normal-stress anisotropy is essential, since this is required to obtain an accurate prediction of the $-\overline{u'v'}$ production, $-P_{12} = \overline{u'u'}\partial\bar{v}/\partial x + \overline{v'v'}\partial\bar{u}/\partial y$.

Close to the surface, the SAYS closure also yields excessive wall-normal stress, with similar negative consequences for the other components. The Π_{22} deficiencies lie mostly in the near-wall correction, via insufficient damping by the function f_{w1}. The DNS budgets also expose the behavior of the turbulent transport D_{ij}^T and dissipation $-\varepsilon_{ij}$, which are best represented by the SAYS closure. The SAYS model is the only one to correctly locate the maximum dissipation of $\overline{u'u'}$ at the wall. This capacity comes at a price, however, in that the SAYS formulation is numerically stiffer than the other two schemes, given that it requires finer spatial and temporal resolution to produce grid-independent results. Its wall-stress history also changes the most when the wall-normal resolution is reduced to a level typical of industrial-flow applications (that is, with the first grid point 0.5 initial wall units off the wall, and 15 points between $y^+ = 0$ and 30). And although the SAYS D_{ij}^T and ε_{ij} models more realistically represent the actual transport and dissipation processes in the strained and unstrained flows, this is not enough to overcome the more serious errors introduced by the P_{ij} and Π_{ij} terms, especially the near-wall modeling deficiencies in the latter. This reiterates the point that rigorous treatment of one or two individual terms does not in and of itself lead to a significant predictive advantage.

5. Summary and closing comments

Three recently proposed Reynolds-stress closures – by Launder–Shima (LS), So et al. (SAYS) and Wilcox (Stress-ω) – have been assessed by applying them to a well-defined perturbed wall-bounded flow, for which DNS

data is available. The DNS benchmark can be viewed as an idealized APG boundary layer, since it involves subjecting fully developed turbulent plane-channel flow to a streamwise deceleration (compression) and wall-normal divergence (stretching) of equal magnitude and opposite sign. We examine both overall performance of the closures and compare their individual terms (and selected combinations) with those from the Reynolds-stress budgets from the DNS. The latter exercise casts light on the validity of the specific modeling assumptions and their practical implications. In particular, we find that the near-wall behavior of all three pressure–strain models is consistently poor. Even more significant, especially from a practical point of view, is the manner in which the individual modeling errors tend to cancel each other, such that the overall closure inaccuracies are much smaller than those in the individual terms – although this error-compensation process is less effective once the flow is subjected to the APG strain.

While all three schemes have their strengths and weaknesses, a case can be made that the overall performance of Stress-ω is better than the other two for the flows considered here, in that its mean-velocity predictions come closest to the DNS. LS and SAYS, on the other hand, are better able to capture the near-wall anisotropy between the streamwise and wall-normal components of the Reynolds stresses.

In general terms, we conclude that besides the inherent advantage of providing statistics that lower-order models do not consider, second-order schemes have the capacity to improve the accuracy of predictions given by less complex closures. However, this potential is not always realized. In fact, for the unstrained channel, of the three closures tested here only Stress-ω significantly improves upon the skin-friction coefficients and mean-velocity profiles given by the one-equation Spalart–Allmaras model and the two-equation SST scheme by Menter. When the APG strain is applied, only Stress-ω is markedly better than SST in its prediction of skin friction, mean velocity and $-\overline{u'v'}$ shear-stress profiles.

A large part of Stress-ω's successful mean-velocity prediction is apparently due to the use by Stress-ω of a transport equation for ω rather than ε. This is suggested by the preliminary study of Sciberras [26], who replaced the ε equations in LS and SAYS with the ω equation used by Stress-ω, and repeated the APG strained-channel comparisons discussed above.[5] The mean-velocities (including the skin friction history and log-law profiles) for both modified closures were better than the original LS and SAYS, for both the strained and unstrained cases, while the normal-stress profiles were comparable to their unmodified results. This implies that addressing the pressure–strain deficiencies highlighted here is not the only (and perhaps not the most important) task facing modelers who would provide the most far-reaching and significant improvements to these and similar closures.

Acknowledgements

We are grateful to Professor Neil Sandham for reviewing the manuscript and offering a number of helpful suggestions. Thanks are also due Professor Ian Castro for his support and encouragement during the course of this work.

Appendix A. Model equations for APG strained-channel flow

Details of the three tested stress-transport closures are presented here. All three schemes are applied to the time-dependent parallel-flow strained-plane-channel geometry. We consider the models in coordinates aligned with the principal axes of the applied irrotational solenoidal deformation A_{ij}, such that the off-diagonal terms are zero. (In order to generalize the following, we assume here the irrotation strain A_{ij} can include non-zero skewing $A_{13} = A_{31}$ and lateral divergence A_{33}, in addition to the APG components A_{11} and A_{22} used above; the following variables thus correspond to the 'starred' quantities x_i^*, u_i^*, A_{ij}^*, etc presented in [2] and [26].) With the aid of the 'deforming' coordinates (η, λ) introduced in Section 2, the Reynolds-stress transport equation (3.1)–(3.2) can be written:

$$\frac{\partial \overline{u_i' u_j'}}{\partial \lambda} = P_{ij} + b^2 \frac{\partial}{\partial \eta}\left(\nu \frac{\partial \overline{u_i' u_j'}}{\partial \eta} \right) + D_{ij}^T + \psi_{ij} + \phi_{ij} - \varepsilon_{ij}, \tag{A.1a}$$

[5] Some of the LS and SAYS model constants were also changed slightly, but not by enough to obscure the basic effects of replacing ε by ω.

where $b = b(\lambda) = \exp(-A_{22}\lambda)$, $\eta = b(\lambda)y$ and the solution is sought (assuming symmetry about the channel centerline) over the lower-half-channel domain, $-h(0) \leqslant \eta \leqslant 0$, corresponding to $-h(t) \leqslant y \leqslant 0$. The total rates of mean strain and rotation for the strained-channel flow are respectively:

$$S_{ij} = \frac{b}{2}\left[\frac{\partial \bar{u}_i}{\partial \eta}\delta_{j2} + \frac{\partial \bar{u}_j}{\partial \eta}\delta_{i2}\right] + A_{ij} \tag{A.1b}$$

(where $S_{ii} = 0$) and (since A_{ij} is irrotational)

$$\Omega_{ij} = \frac{b}{2}\left[\frac{\partial \bar{u}_i}{\partial \eta}\delta_{j2} - \frac{\partial \bar{u}_j}{\partial \eta}\delta_{i2}\right]. \tag{A.1c}$$

The production term $P_{ij} = -\overline{u_i'u_k'}\partial\bar{u}_j/\partial x_k - \overline{u_j'u_k'}\partial\bar{u}_i/\partial x_k$ reduces to $P_{ij} = P_{ij}^S + P_{ij}^A$ where:

$$P_{ij}^S = -\overline{u_i'v'}b\frac{\partial \bar{u}_j}{\partial \eta} - \overline{u_j'v'}b\frac{\partial \bar{u}_i}{\partial \eta}, \tag{A.1d}$$

and

$$P_{ij}^A = -\overline{u_i'u_k'}A_{jk} - \overline{u_j'u_k'}A_{ik}. \tag{A.1e}$$

No-slip boundary conditions are assumed, i.e. $\overline{u_i'u_j'} = 0$ at $\eta_w = 0$, where $\eta_w = b(t)[h(t) + y]$. At $\eta_w = h(0)$ (the centerline), zero derivatives[6] of $\overline{u_i'u_j'}$ are imposed except for the Reynolds shear stresses $-\overline{u'v'}$ and $-\overline{v'w'}$, which are themselves set to zero. Therefore, at the 'top' (centerline) of the strained domain $\eta_w/h(0) = 1$:

$$\frac{\partial\overline{u'w'}}{\partial\eta} = \frac{\partial\overline{u'u'}}{\partial\eta} = \frac{\partial\overline{v'v'}}{\partial\eta} = \frac{\partial\overline{w'w'}}{\partial\eta} = 0 \quad \text{and} \quad -\overline{u'v'} = -\overline{v'w'} = 0.$$

Differences between the closures lie in the assumptions made for the turbulent transport D_{ij}^T, pressure-gradient-velocity correlation $\Pi_{ij} = \psi_{ij} + \phi_{ij}$ (or its constituents, the pressure-transport ψ_{ij} and pressure–strain ϕ_{ij} terms) and dissipation tensor ε_{ij}, and in the 'extra' variable, ε or ω, used to define the time scale and close the equation set.

Launder–Shima closure (LS) [12]:
Models:

$$D_{ij}^T + \psi_{ij} = b^2\frac{\partial}{\partial\eta}\left(C_s\frac{k}{\varepsilon}\overline{v'v'}\frac{\partial\overline{u_i'u_j'}}{\partial\eta}\right), \tag{A.2a}$$

$$\varepsilon_{ij} = \frac{2}{3}\varepsilon\delta_{ij}, \tag{A.2b}$$

$$\phi_{ij} = \phi_{ij}^S + \phi_{ij}^R + \phi_{ij\,W}^S + \phi_{ij\,W}^R,$$

with:

$$\begin{aligned}
\phi_{ij}^S &= -c_1\varepsilon a_{ij},\\
\phi_{ij}^R &= -c_2\left(P_{ij} - \frac{2}{3}\mathcal{P}\delta_{ij}\right),\\
\phi_{ij\,W}^S &= c_1^w\frac{\varepsilon}{k}\left(\overline{v'v'}\delta_{ij} - \frac{3}{2}\overline{v'u_i'}\delta_{j2} - \frac{3}{2}\overline{v'u_j'}\delta_{i2}\right)f,\\
\phi_{ij\,W}^R &= c_2^w\left(\phi_{22}^R\delta_{ij} - \frac{3}{2}\phi_{i2}^R\delta_{j2} - \frac{3}{2}\phi_{j2}^R\delta_{i2}\right)f.
\end{aligned} \tag{A.2c}$$

[6] A second-order zero derivative approximation is used, to avoid introducing inaccuracies in the history of the mean centerline-wall velocity difference imposed by (2.3).

Auxiliary functions:

$$\mathcal{P} = \frac{1}{2}P_{kk}, \quad f = \frac{0.4\,b\,k^{3/2}}{\varepsilon\eta_{\mathrm{w}}}, \qquad a_{ij} = \left(\overline{u_i'u_j'} - \frac{2}{3}k\delta_{ij}\right)\Big/k,$$
$$A_2 = a_{ik}a_{ki}, \quad A_3 = a_{ik}a_{kj}a_{ji}, \quad A = \left[1 - \frac{9}{8}(A_2 - A_3)\right],$$
$$R_t = \frac{k^2}{\nu\varepsilon},$$
$$c_1 = 1 + 2.58AA_2^{1/4}\left(1 - \exp\left[-(0.0067R_t)^2\right]\right),$$
$$c_2 = 0.75A^{1/2},$$
$$c_1^w = -\frac{2}{3}c_1 + 1.67,$$
$$c_2^w = \max\left[\left(\frac{2}{3}c_2 - \frac{1}{6}\right)\Big/c_2, 0\right]. \tag{A.2d}$$

Additional transport equation:

$$\frac{\partial\varepsilon}{\partial\lambda} = b^2\frac{\partial}{\partial\eta}\left[\left(C_\varepsilon\frac{k}{\varepsilon}\overline{v'v'} + \nu\right)\frac{\partial\varepsilon}{\partial\eta}\right] + (C_{\varepsilon1} + \varphi_1 + \varphi_2)\frac{\varepsilon}{k}\mathcal{P} - C_{\varepsilon2}\frac{\varepsilon\bar{\varepsilon}}{k}. \tag{A.2e}$$

Auxiliary functions:

$$\bar{\varepsilon} = \varepsilon - 2\nu b^2\left(\frac{\partial k^{1/2}}{\partial\eta}\right)^2,$$
$$\varphi_1 = 2.5A\left(\frac{\mathcal{P}}{\varepsilon} - 1\right),$$
$$\varphi_2 = 0.3(1 - 0.3A_2)\exp\left[-(0.002R_t)^2\right]. \tag{A.2f}$$

Boundary conditions:

$$\varepsilon_w = 2\nu b^2\left(\frac{\partial k^{1/2}}{\partial\eta}\right)^2 \quad \text{at } \eta_{\mathrm{w}} = 0; \qquad \frac{\partial\varepsilon}{\partial\eta} = 0 \quad \text{at } \eta_{\mathrm{w}} = h(0). \tag{A.2g}$$

LS constants: $C_s = 0.2$, $C_\varepsilon = 0.18$, $C_{\varepsilon1} = 1.45$, $C_{\varepsilon2} = 1.9$.

So, Aksoy, Yuan and Sommer closure (SAYS) [13]:

Models:

$$D_{ij}^T = b^2\frac{\partial}{\partial\eta}\left[C_s\frac{k}{\varepsilon}\left(\overline{u_i'v'}\frac{\partial\overline{u_j'v'}}{\partial\eta} + \overline{u_j'v'}\frac{\partial\overline{v'u_i'}}{\partial\eta} + \overline{v'v'}\frac{\partial\overline{u_i'u_j'}}{\partial\eta}\right)\right], \tag{A.3a}$$

$$\varepsilon_{ij} = \frac{2}{3}\varepsilon\delta_{ij} + f_{w1}\frac{\varepsilon}{k}\left[-\frac{2}{3}k\delta_{ij} + \frac{\overline{u_i'u_j'} + \overline{u_i'v'}\delta_{j2} + \overline{u_j'v'}\delta_{i2} + \overline{v'v'}\delta_{i2}\delta_{j2}}{1 + \frac{3}{2}\overline{v'v'}/k}\right], \tag{A.3b}$$

$$\Pi_{ij} = \phi_{ij} + \psi_{ij} = -\left(C_1\varepsilon + C_1^*\mathcal{P}\right)b_{ij} + C_2\varepsilon\left(b_{ik}b_{kj} - \frac{1}{3}\Pi\delta_{ij}\right) - \alpha_1\left(P_{ij} - \frac{2}{3}\mathcal{P}\delta_{ij}\right)$$
$$- \beta_1\left(D_{ij} - \frac{2}{3}\mathcal{P}\delta_{ij}\right) - \left(2\gamma_1 + C_3^*\Pi^{1/2}\right)kS_{ij} + \phi_{ij}^W + \psi_{ij},$$

with

$$\phi_{ij}^W = f_{w1}\left[\left(C_1\varepsilon + C_1^*\mathcal{P}\right)b_{ij} - C_2\varepsilon\left(b_{ik}b_{kj} - \frac{1}{3}\Pi\delta_{ij}\right) + \alpha^*\left(P_{ij} - \frac{2}{3}\mathcal{P}\delta_{ij}\right) + 2\gamma^*kS_{ij}\right],$$
$$\psi_{ij} = -\frac{b^2}{3}\left[\frac{\partial}{\partial\eta}\left(\nu\frac{\partial\overline{u_i'v'}}{\partial\eta}\right)\delta_{j2} + \frac{\partial}{\partial\eta}\left(\nu\frac{\partial\overline{u_j'v'}}{\partial\eta}\right)\delta_{i2}\right] + \frac{b^2}{3}\frac{\partial}{\partial\eta}\left(\nu\frac{\partial\overline{v'v'}}{\partial\eta}\right)\delta_{i2}\delta_{j2}. \tag{A.3c}$$

Auxiliary functions:

$$b_{ij} = \frac{1}{2k}\left(\overline{u_i' u_j'} - \frac{2}{3}k\delta_{ij}\right),$$
$$D_{ij} = -\left[\overline{u_i' u_k'}\left(b\frac{\partial \bar{u}_k}{\partial \eta}\delta_{j2} + A_{kj}\right) + \overline{u_j' u_k'}\left(b\frac{\partial \bar{u}_k}{\partial \eta}\delta_{i2} + A_{ki}\right)\right],$$
$$\mathcal{P} = \frac{1}{2}P_{kk}, \quad \Pi = b_{ij}b_{ij}, \quad R_t = \frac{k^2}{\nu\varepsilon},$$
$$f_{w1} = \exp\left[-(R_t/200)^2\right]. \tag{A.3d}$$

Additional transport equation:

$$\frac{\partial \varepsilon}{\partial \lambda} = b^2\frac{\partial}{\partial \eta}\left[\left(C_\varepsilon\frac{k}{\varepsilon}\overline{v'v'} + \nu\right)\frac{\partial \varepsilon}{\partial \eta}\right] + C_{\varepsilon 1}\frac{\varepsilon}{k}\mathcal{P} - C_{\varepsilon 2}\frac{\varepsilon\bar{\varepsilon}}{k} + \xi. \tag{A.3e}$$

Auxiliary functions:

$$\xi = f_{w2}\left(-N\frac{\varepsilon\bar{\varepsilon}}{k} + M\frac{\varepsilon^{*2}}{k} - L\frac{\varepsilon}{k}\mathcal{P}\right),$$
$$\bar{\varepsilon} = \varepsilon - 2\nu b^2\left(\frac{\partial k^{1/2}}{\partial \eta}\right)^2,$$
$$\varepsilon^* = \varepsilon - 2\nu b^2\frac{k}{\eta^2},$$
$$f_{w2} = \exp\left[-(R_t/40)^2\right]. \tag{A.3f}$$

Boundary conditions:

$$\varepsilon_w = 2\nu b^2\left(\frac{\partial k^{1/2}}{\partial \eta}\right)^2 \quad \text{at } \eta_w = 0; \qquad \frac{\partial \varepsilon}{\partial \eta} = 0 \quad \text{at } \eta_w = h(0). \tag{A.3g}$$

SAYS constants: $C_s = 0.11$, $C_1 = 3.4$, $C_2 = 4.2$, $C_1^* = 1.8$, $C_3^* = 1.3$, $\alpha_1 = 0.4125$, $\beta_1 = 0.2125$, $\gamma_1 = 0.01667$, $\alpha^* = -0.29$, $\gamma^* = 0.065$, $C_\varepsilon = 0.12$, $C_{\varepsilon 1} = 1.5$, $C_{\varepsilon 2} = 1.83$, $L = 2.25$, $M = 0.5$, $N = 0.57$.

Wilcox Stress-ω closure [14]:

Models:

$$D_{ij}^T + \psi_{ij} = b^2\frac{\partial}{\partial \eta}\left(\sigma^*\nu_T\frac{\partial \overline{u_i' u_j'}}{\partial \eta}\right), \tag{A.4a}$$
$$\varepsilon_{ij} = \frac{2}{3}\beta^*\omega k\delta_{ij}, \tag{A.4b}$$
$$\phi_{ij} = -\beta^* C_1\omega\left(\overline{u_i' u_j'} - \frac{2}{3}k\delta_{ij}\right) - \hat{\alpha}\left(P_{ij} - \frac{2}{3}\mathcal{P}\delta_{ij}\right) - \hat{\beta}\left(D_{ij} - \frac{2}{3}\mathcal{P}\delta_{ij}\right) - \hat{\gamma}kS_{ij}. \tag{A.4c}$$

Auxiliary functions:

$$D_{ij} = -\left[\overline{u_i' u_k'}\left(b\frac{\partial \bar{u}_k}{\partial \eta}\delta_{j2} + A_{kj}\right) + \overline{u_j' u_k'}\left(b\frac{\partial \bar{u}_k}{\partial \eta}\delta_{i2} + A_{ki}\right)\right],$$
$$\mathcal{P} = \frac{1}{2}P_{kk}, \quad \nu_T = \alpha^*\frac{k}{\omega}, \quad R_t = \frac{k}{\omega\nu},$$
$$\alpha^* = \frac{\alpha_0^* + R_t/R_k}{1 + R_t/R_k}, \qquad \chi_k = \frac{b^2}{\omega^3}\frac{\partial k}{\partial \eta}\frac{\partial \omega}{\partial \eta},$$
$$\beta^* = \beta_\infty^*\left(\frac{4/15 + R_t/R_\beta}{1 + R_t/R_\beta}\right)f_{\beta *}, \qquad f_{\beta *} = \begin{cases} 1 & \text{if } \chi_k \leqslant 0 \\ \frac{1+640\chi_k^2}{1+400\chi_k^2} & \text{if } \chi_k > 0, \end{cases}$$

$$\hat{\alpha} = \frac{1+\hat{\alpha}_\infty R_t/R_k}{1+R_t/R_k}, \quad \hat{\beta} = \hat{\beta}_\infty \frac{R_t/R_k}{1+R_t/R_k}, \quad \hat{\gamma} = \hat{\gamma}_\infty \frac{\hat{\gamma}_0 + R_t/R_k}{1+R_t/R_k},$$
$$C_1 = \frac{9}{5}\left(\frac{5/3+R_t/R_k}{1+R_t/R_k}\right),$$
$$\hat{\alpha}_\infty = \frac{8+C_2}{11}, \quad \hat{\beta}_\infty = \frac{8C_2-2}{11}, \quad \hat{\gamma}_\infty = \frac{60C_2-4}{55}, \quad \alpha_0^* = \frac{1}{3}\beta_0. \tag{A.4d}$$

Additional transport equation:

$$\frac{\partial \omega}{\partial \lambda} = -\alpha \frac{\omega}{k}\left(\overline{u_k' v'}\, b\, \frac{\partial \bar{u}_k}{\partial \eta} + \overline{u_k' u_\ell'} A_{k\ell}\right) - \beta\omega^2 + b^2 \frac{\partial}{\partial \eta}\left[(\nu + \sigma \nu_T)\frac{\partial \omega}{\partial \eta}\right]. \tag{A.4e}$$

Auxiliary functions:

$$\alpha = \frac{13}{25}\left(\frac{\alpha_0 + R_t/R_\omega}{1+R_t/R_\omega}\right)\left(\frac{3+R_t/R_\omega}{3\alpha_0^*+R_t/R_\omega}\right), \qquad \chi_\omega = \left|\frac{\Omega_{ij}\Omega_{jk}S_{ki}}{(\beta_\infty^*\omega)^3}\right|,$$
$$f_\beta = \frac{1+70\chi_\omega}{1+80\chi_\omega}, \qquad \beta = \beta_0 f_\beta. \tag{A.4f}$$

Boundary conditions:

$$\omega = \frac{6\nu b^2}{\beta_0 \eta_w^2} \quad \text{below } \eta_w u_\tau(0)/\nu = 1.4;$$
$$\frac{\partial \omega}{\partial \eta} = 0 \quad \text{at } \eta_w = h(0). \tag{A.4g}$$

Stress-ω constants: $\sigma^* = 0.5$, $\sigma = 0.5$, $C_2 = 0.52$, $\beta_\infty^* = 0.09$, $\beta_0 = 0.072$, $\alpha_0 = 0.105$, $\hat{\gamma}_0 = 0.007$, $R_\beta = 12$, $R_k = 12$, $R_\omega = 6.2$.

References

[1] C.P. Yorke, G.N. Coleman, Assessment of common turbulence models for an idealised adverse pressure gradient flow, Eur. J. Mech. B Fluids 23 (2004) 319.
[2] G.N. Coleman, J. Kim, P.R. Spalart, A numerical study of strained three-dimensional wall-bounded turbulence, J. Fluid Mech. 416 (2000) 75.
[3] G.N. Coleman, J. Kim, P.R. Spalart, Direct numerical simulation of a decelerated wall-bounded turbulent shear flow, J. Fluid Mech. 495 (2003) 1.
[4] P.R. Spalart, J.H. Watmuff, Experimental and numerical study of a turbulent boundary layer with pressure gradients, J. Fluid Mech. 249 (1993) 337.
[5] Y. Nagano, T. Tsuji, T. Houra, Structure of turbulent boundary layer subjected to adverse pressure gradient, in: Proceedings of the Eleventh Symposium on Turbulent Shear Flows, September 1997, pp. 33.7–33.12.
[6] A.E. Alving, H.H. Fernholz, Mean-velocity scaling in and around a mild, turbulent separation bubble, Phys. Fluids 7 (1995) 1956.
[7] W.M. Kays, M.E. Crawford, Convective Heat and Mass Transfer, third ed., McGraw-Hill, 1993.
[8] R.S. Rogallo, Numerical experiments in homogeneous turbulence, NASA TM 81315 (1981). Available from NASA Scientific & Technical Information, help@sti.nasa.gov.
[9] M.J. Lee, W.C. Reynolds, Numerical experiments on the structure of homogeneous turbulence, Mech. Engrg. Dept., Stanford University, Thermosci. Div. Rep. TF-24, November 1985.
[10] J.L. Lumley, The pressure–strain correlation, Phys. Fluids 18 (1975) 750.
[11] S.B. Pope, Turbulent Flows, Cambridge University Press, 2000.
[12] B.E. Launder, N. Shima, Second-moment closure for the near-wall sublayer: development and application, AIAA J. 27 (1989) 1319.
[13] R.M.C. So, H. Aksoy, S.P. Yuan, T.P. Sommer, Modeling Reynolds-number effects in wall-bounded turbulent flows, J. Fluids Engrg. 118 (1996) 260.
[14] D.C. Wilcox, Turbulence Modeling for CFD, second ed., DCW Industries, 1998.
[15] C.G. Speziale, S. Sarkar, T.B. Gatski, Modeling the pressure–strain correlation of turbulence: an invariant dynamical systems approach, J. Fluid. Mech. 227 (1991) 245.
[16] M.M. Gibson, B.E. Launder, Ground effects on pressure fluctuations in the atmospheric boundary layer, J. Fluid Mech. 86 (1978) 491.
[17] B.J. Daly, F.H. Harlow, Transport equations in turbulence, Phys. Fluids 13 (1970) 2634.
[18] A.N. Kolmogorov, Local structure of turbulence in incompressible viscous fluids for very large Reynolds number, Dokl. Akad. Nauk SSSR 30 (1941) 299.
[19] J.L. Lumley, Computational modeling of turbulent flows, Adv. Appl. Mech. 18 (1978) 123.

[20] J.L. Lumley, Second-order modeling of turbulent flows, in: W. Kollmann (Ed.), Prediction Methods for Turbulent Flows, Hemisphere, New York, 1980, p. 1.
[21] K. Hanjalic, B.E. Launder, A Reynolds-stress model of turbulence and its application to thin shear flows, J. Fluid Mech. 52 (1972) 609.
[22] Y.G. Lai, R.M.C. So, On near-wall turbulent flow modelling, J. Fluid. Mech. 211 (1991) 641.
[23] B.E. Launder, W.C. Reynolds, Asymptotic near-wall stress dissipation rates in a turbulent flow, Phys. Fluids 26 (1983) 1157.
[24] S.P. Yuan, R.M.C. So, A near-wall Reynolds-stress closure with out wall normals. NASA Contractor Report 4785, July 1997.
[25] B.E. Launder, G.J. Reece, W. Rodi, Progress in the development of a Reynolds-stress turbulence closure, J. Fluid Mech. 68 (1975) 537.
[26] M.A. Sciberras, Assessment of Reynolds-stress closures applied to two- and three-dimensional wall-bounded turbulence, Univ. of Southampton, Sch. Engrg. Sci., Aerodyn. & Flight Mech. Res. Group Tech. Rep. AFM-05/03, December 2005.
[27] R.M.C. So, Y.G. Lai, H.S. Zhang, B.C. Hwang, Second-order near-wall turbulence closures: a review, AIAA J. 29 (1991) 1819.
[28] M.A. Sciberras, G.N. Coleman, Testing of Reynolds-stress-transport closures by comparison with DNS of an idealized adverse-pressure-gradient boundary layer, Univ. of Southampton, Sch. Engrg. Sci., Aerodyn. & Flight Mech. Res. Group Tech. Rep. AFM-06/01, May 2006.
[29] R.D. Moser, J. Kim, N.N. Mansour, Direct numerical simulation of turbulent channel flow up to $Re_\tau = 590$, Phys. Fluids 11 (1999) 943.
[30] A.O. Demuren, S. Sarkar, Perspective: systematic study of Reynolds stress closure models in the computation of plane channel flows, Trans. ASME: J. Fluids Engrg. 115 (1993) 5.
[31] N.N. Mansour, J. Kim, P. Moin, Reynolds-stress and dissipation-rate budgets in a turbulent channel flow, J. Fluid Mech. 194 (1988) 15.